AREA DEPENDENCE OF JOSEPHSON CRITICAL CURRENT DENSITY IN SUPERCONDUCTING $Bi_2Sr_2CaCu_2O_{8+d}$ MESAS FOR TERAHERTZ EMISSION

A Thesis submitted to
the Graduate School of Engineering and Sciences of
İzmir Institute of Technology
in Partial Fulfillment of the Requirements for the Degree of

MASTER OF SCIENCE

in Physics

by
Hilal SAĞLAM

June 2013
İZMİR

We approve the thesis of **Hilal SAĞLAM**

Examining Committee Members:

Prof. Dr. Lütfi ÖZYÜZER
Department of Physics, İzmir Institute of Technology

Prof. Dr. Ekrem YANMAZ
Department of Physics, Karadeniz Technical University

Prof. Dr. Birol ENGİN
Department of Physics, 9 Eylül University

4 June 2013

Prof. Dr. Lütfi ÖZYÜZER
Supervisor, Department of Physics
Izmir Institute of Technology

Prof. Dr. Nejat BULUT
Head of the Department of Physics

Prof. Dr. R. Tuğrul SENGER
Dean of the Graduate School of
Engineering and Sciences

ACKNOWLEDGMENTS

I am certain that this acknowledgment page is woefully incomplete; however, I will do my best to list the people who helped me during the three years of my M.S. studies. At the top of the list, I would like to thank my supervisor Prof. Lütfi ÖZYÜZER for letting my thesis grow under his supervision and asking many incisive questions which cut through a great deal of woolly thinking and sharpen my opinions to get to the important points of terahertz science and technology and his vast knowledge and experience played a key role in completing this thesis successfully. Furthermore, I acknowledge him since he was always willing to help me during my experiments in spite of his hectic schedule.

I would also like to acknowledge Prof. Kadowaki from University of Tsukuba and Prof. Miyakawa from Tokyo University of Science for providing the Bi2212 crystals. In addition, I appreciate the thesis committee members Prof. Ekrem YANMAZ and Prof. Birol ENGİN for their comments on my thesis.

Thanks also to Yasemin DEMİRHAN for a huge amount of technical help and for her patience in the face of my repeated questions about superconductivity and terahertz science. Furthermore, I am grateful to Adnan TAŞDEMİR for supporting me many times while the schematics of the experimental processes were being drawn. Because, without his endless help it would take too much time to complete this thesis.

Within the list of close collaborators, I am very thankful to my all group members for providing me endless hours of entertainment and useful discussions. In addition, I would like to thank to all my friends at IZTECH for the great atmosphere while I was studying.

I acknowledge TUBITAK (Scientific and Technical Research Council of Turkey) since this project is supported by TUBITAK with project number 110T248 and thanks also to AQUREC (Applied Quantum Research Center) at IZTECH for providing me clean room facilities such as e-beam lithography system.

Needless to say, my friends; Şeyma ULUSOY UYANIK and Duygu COŞAN have provided immeasurable support and letting me feel their sincere love over the last 3 years of my M. S. studies.

Finally, particular thanks to my family, who has experienced all the highs and lows of my studies and this thesis would not have been possible without them.

ABSTRACT

AREA DEPENDENCE OF JOSEPHSON CRITICAL CURRENT DENSITY IN SUPERCONDUCTING $Bi_2Sr_2CaCu_2O_{8+d}$ MESAS FOR TERAHERTZ EMISSION

There are numerous application fields of terahertz waves such as airport screening of passengers for weapons, explosives, drugs, secure wireless communications, cancer detection, etc. high-T_c superconductor $Bi_2Sr_2CaCu_2O_{8+\delta}$ (Bi2212) single crystal has been observed as an intense, coherent, continuous electromagnetic wave source in terahertz frequency region. Bi2212, which is highly anisotropic high-T_c superconductor, is considered as a stack of intrinsic Josephson junctions (IJJs) on atomic scale. In this study, we have fabricated triple mesa structures on a same chip with various mesa areas (300×50, 200×50, 100×50 μm^2). Firstly, single crystal of Bi2212 is glued onto a sapphire substrate from its smooth a-b surface by silver epoxy. After deposition of 100 nm Au layer, rectangular mesa structures were fabricated on the surface of an under-doped Bi2212 crystal by using e-beam lithography and Ar-ion etching step by step. On account of the difficulties in making a contact on small area of the mesa, CaF_2 insulating layer deposition was performed. After that, a gold stripe with the width of 30 μm was created by lift-off technique on the mesa and CaF_2 layer. Finally, three gold probe wires were connected to the two contact paths and mesa by silver epoxy. After the mesa fabrication, the exact dimensions of the mesas were obtained using atomic force microscope. To obtain the electrical characterization, c-axis resistance versus temperature (R-T), and current-voltage behavior (I-V) were measured. From I-V characteristics, critical current of each mesa structure having different dimension was obtained, after that, we have calculated the critical current densities of each mesa structure and then we have studied change in Josephson critical current density of mesas with different dimensions. We can conclude from the I-V measurements of the mesas that the Josephson critical current density is decreasing when the area of mesa is increasing. Furthermore, the backbending voltage points are increasing since heating effects dominate for the large areas of the mesa structures.

ÖZET

TERAHERTZ IŞIYAN SÜPERİLETKEN $Bi_2Sr_2CaCu_2O_{8+d}$ MESALARIN JOSEPHSON KRİTİK AKIM YOĞUNLUĞUNUN ALANA BAĞIMLILIĞI

Terahertz dalgaları, yolcuların havaalanında taranması, patlayıcı ve ilaç tayini, güvenli kablosuz iletişim ve tıpta kanser tanısı gibi bir çok alanda önemli uygulama alanina sahiptir. Yakın bir zaman önce, $Bi_2Sr_2CaCu_2O_{8+d}$ (Bi2212) tek kristallerinden yapılan mesaların, küçük boyutlu bir kaynak olarak yüksek güçte terahertz ışıması yapabildiği kanıtlanmıştır. Katmanlı yüksek sıcaklık süperiletkeni Bi2212, özgün Josephson eklemleri olarak adlandırılan Josephson eklemlerinin doğal yığınlarına sahiptir. Terahertz ışıması, elektromagnetik spektrumun mikrodalgalar ile uzak-IR arasında yer alan bir bölümüdür. Bu bölge 0.1-10 THz frekans aralığına ve 3 mm den 0,03 mm ye dalga boyu aralığına sahiptir. Bu çalışmada farklı alanlara sahip (300×50, 200×50, 100×50 μm^2) mesa yapıları aynın kristal üzerinde oluşturulmuştur. İlk once tavlanmış olan kristaller safir altaş üzerine yapıştırılmıştır ve ardından cleave işlemi gerçekleştirilmiştir. Daha sonra 100 nm kalınlığında altın kaplanmıştır ve ardından e-demeti litrografi tekniği ile Ar iyon demeti aşındırma yöntemleri kullanılarak üçlü mesa yapıları elde edilmiştir. Üretilen mesaların alanları çok küçük olduğundan dolayı, elektriksel ölçüm almak için oluşturulacak kontakları kolaylaştırmak amacıyla CaF_2 yalıtkan tabaksı kaplanmıştır. En son olarakta gümüş epoksi kullanılarak kontaklar alınmıştır. Mesa üretimi tamamlandıktan sonra SEM ve yüzey profilometrisi kullanılarak üretilen mesaların tam boyutları tayin edilmiştir. Elektriksel karakterizayonu için ise R-T ve I-V ölçümleri alınmıştır. I-V karakteristiklerine bakılarak her bir mesa için kritik akım değerleri tayin edilerek, Josephson kritik akım yoğunlukları hesaplanmıştır. Çalışmanın sonucunda Josephson kritik akım yoğunluğunun mesa alanının artmasıyla azaldığı gözlenmiştir. Dahası, yüksek boyutlu mesalarda ısınma etkilerinin baskın olmasından dolayı, akım gerilim grafiklerinde geri bükülme değerleri daha düşük voltajlarda gözlenmiştir.

To My Family

TABLE OF CONTENTS

LIST OF FIGURES ix

LIST OF TABLES xii

CHAPTER 1. TERAHERTZ WAVES 1

1.1. Terahertz Band 1

1.2. Application Areas of Terahertz Radiation 2

1.3. Terahertz Generation 6

1.4. THz Generation from HTS Superconductor $Bi_2Sr_2CaCu_2O_{8+d}$ 8

1.5. Terahertz Detection 13

CHAPTER 2. THEORETICAL BACKGROUND 17

2.1. Introduction 17

2.2. A Brief History of Superconductivity 18

2.3. Superconducting Materials 19

2.4. Characteristic Properties of Superconductors 20

2.5. The BCS Mechanism 21

2.6. Type I and Type II Superconductors 23

2.6.1. Type II Superconductor: Bi2212 25

2.7. Tunneling Process 27

2.7.1. Normal Metal-Insulator-Normal Metal Tunneling 27

2.7.2. Normal Metal-Insulator-Superconductor Tunneling 28

2.7.3. Superconductor-Insulator-Superconductor Tunneling 29

2.8. Josephson Junctions 31

2.9. Doping Dependence of Bi2212 Single Crystal 34

2.10. Objective of the Work 37

CHAPTER 3. EXPERIMENTAL 38

3.1. Annealing of Bi2212 Single Crystal 38

3.2. Mesa Fabrication Process 40

3.2.1. Thermal Evaporation 40

3.2.2. E-beam Lithography Process 42
3.3.3. Ion Beam Etching 44
3.3.4. Gold Stripe Fabrication 46
3.3.5. R-T, I-V and Golay cell Measurements 47

CHAPTER 4. RESULTS AND DISCUSSION 50
4.1. Structural Characterization 50
4.1.1. Optic Microscope Images 50
4.1.2. SEM and Profilometer Results 52
4.2. Electrical Measurement Results 56
4.2.1. Temperature Dependence of c-axis Resistance in Bi2212 56
4.2.2. Tunneling Characteristic of Bi2212 Single Crystal 65

CHAPTER 5. CONCLUSION 73

REFERENCES 75

LIST OF FIGURES

Figure **Page**

Figure 1.1. The electromagnetic spectrum with THz gap 2

Figure 1.2. Applications of terahertz imaging in security inspections, medical diagnosis and industrial quality control 4

Figure 1.3. Optical properties of condensed matter in the THz band 4

Figure 1.4. Application of terahertz radiation 5

Figure 1.5. Conduction band structure of THz quantum cascade lasers 8

Figure 1.6. Schematic diyagram of mesa from Bi2212 crystal for terahertz emission .. 10

Figure 1.7. Coherent detection of terahertz radiation 14

Figure 1.8. Bolometer detector 15

Figure 1.9. Golay cell 16

Figure 2.1. The first introduce of superconductivity by Ones in 1911 18

Figure 2.2. The timeline of discovery of superconducting materials 20

Figure 2.3. Meissner effect 22

Figure 2.4. A model of Cooper pair attraction 22

Figure 2.5. Type 1 and Type 2 superconductors 23

Figure 2.6. Crystal structure of Bi2212 and crystal structure from x-ray diffraction 26

Figure 2.7. Normal metal-insulator-normal metal tunneling 27

Figure 2.8. Normal metal-insulator-superconductor tunneling 28

Figure 2.9. I-V characteristics of normal metal-insulator-superconductor tunneling 29

Figure 2.10. Superconductor-insulator-superconductor tunneling 30

Figure 2.11. I-V characteristics of superconductor-insulator-superconductor tunneling 30

Figure 2.12. The phase diagram with doping in high-Tc cuprates superconductors 36

Figure 2.13. c-axis resistivity of $Bi_2Sr_2CaCu_2O_{8+d}$ versus temperature for different doping levels 36

Figure 3.1. Our annealing system in Argon atmosphere 39

Figure 3.2. Annealing system under vacuum 39

Figure 3.3. The steps in the beginning for the mesa fabrication a) Adhesion of crystal on substrate b) Cleaving crystal c) Gold layer deposition on crystal 41

Figure 3.4. Schematic of our thermal evaporation system 42

Figure 3.5. Picture of our electron beam lithography system 43

Figure 3.6. Schematic representation of e-beam lithography processes 44
Figure 3.7. Schematic picture of our ion beam etching system 45
Figure 3.8. Schematic of triple mesa structure 46
Figure 3.9. a) CaF_2 deposition onto crystal and small part of mesa b) Gold stripe deposition on mesa and CaF_2 layer 46
Figure 3.10. The final measurement configuration of mesa structure 47
Figure 3.11. The schematic of our He flow cryostat system 48
Figure 4.1. Optical images of crystals before and after annealing 51
Figure 4.2. Optical images of HS14 after mesa fabrication 51
Figure 4.3. Optical image of HS14 after gold stripe fabrication by lift off technique ... 51
Figure 4.4. Optical images of HS02 52
Figure 4.5. SEM images of HS14 52
Figure 4.6. SEM images of HS14 53
Figure 4.7. SEM images of HS02 53
Figure 4.8. Step-height analyses of HS02 54
Figure 4.9. Resistance versus temperature behavior of HS01a 58
Figure 4.10. Resistance versus temperature behavior of HS01b 59
Figure 4.11. Resistance versus temperature behavior of HS01c 59
Figure 4.12. Resistance versus temperature behavior of all samples together 60
Figure 4.13. Resistance versus temperature behavior of HS02a 60
Figure 4.14. Resistance versus temperature behavior of HS02b 61
Figure 4.15. Resistance versus temperature behavior of HS02c 61
Figure 4.16. Resistance versus temperature behavior of all samples together 62
Figure 4.17. Resistance versus temperature behavior of HS11a 62
Figure 4.18. Resistance versus temperature behavior of HS11b 63
Figure 4.19. Resistance versus temperature behavior of HS11c 63
Figure 4.20. Resistance versus temperature behavior of all samples together 64
Figure 4.21. I-V measurement of HS01a at 20 K 65
Figure 4.22. I-V measurement of HS01b at 20K 66
Figure 4.23. I-V measurement of HS01c at 20K 66
Figure 4.24. I-V measurement of HS02a at 20K 68
Figure 4.25. I-V measurement of HS02b at 20K 68
Figure 4.26. I-V measurement of HS02c at 20K 69
Figure 4.27. I-V measurement of HS11a at 20K 70

Figure 4.28. I-V measurement of HS11b at 20K 70
Figure 4.29. I-V measurement of HS11c at 20K 71

LIST OF TABLES

Table **Page**

Table 4.1. Height of mesas and deposited thin films for HS01……...64
Table 4.2. Height of mesas and deposited thin films for HS02…….....65
Table 4.3. Height of mesas and deposited thin films for HS11……...65
Table 4.4. Electrical properties of HS01……..……...67
Table 4.5. Electrical properties of HS02……..……...67
Table 4.6. Electrical properties of HS11……..……...78
Table 4.7. I-V characteristics of HS01 ……..…….78
Table 4.8. I-V characteristics of HS02……..……..80
Table 4.9. I-V characteristics of HS11 ……..…….82

CHAPTER 1

TERAHERTZ WAVES

1.1. Terahertz Band

Electromagnetic waves and their effects are very important in science and technology since they have many impacts on human-being lives in various ways. Electromagnetic radiation can be easily used in the form of energy and also makes easy carrying of informative data. As it is seen in the Figure 1.1, the electromagnetic wave spectrum extends from very short wavelengths such as X-rays to very long wavelengths such as radio waves. Whereas long wavelengths are used for communications, TV and radio broadcasting, short wavelengths are generally used for medical imaging applications such as x-ray tomography. Until recently, one region of the electromagnetic spectrum, the terahertz (THz) region that lies between microwaves and infra-red, has remained a mystery. The electromagnetic spectrum with terahertz gap can be seen in Figure 1.1. However, the terahertz gap has been speedily decreasing for the last ten years since many scientists made tremendous achievements about this gap. In addition, the region in which electromagnetic physics can be best described by its wave-like characteristics (microwave) and its particle-like characteristics (infrared). Furthermore, the terahertz spectral regime is ranging between 0.1 THz and 10 THz and 1 THz corresponds to a scale of 1 ps, a wavelength of 300 μm, an electron energy of 4.1 meV and temperature of 47.6 K.

Terahertz radiations have unique properties; these radiations are non-ionizing like infrared radiation and as microwave radiation, they can penetrate through many materials such as plastics, wood, ceramics etc. In addition, the penetration depth is typically in the range of microwave. However, terahertz radiations have difficulty in penetrating through fog and clouds and they cannot penetrate through metallic objects and liquid water.

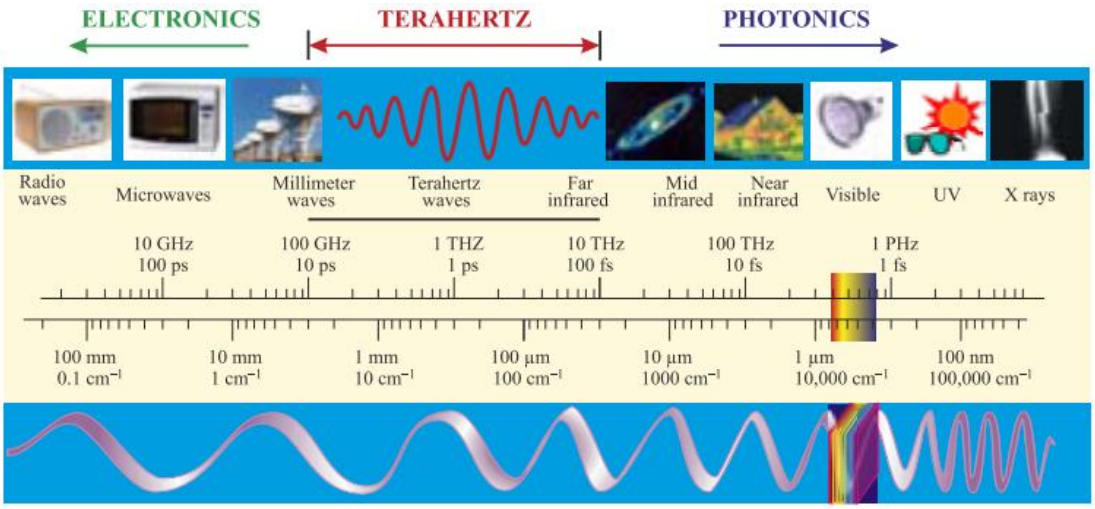

Figure 1.1. The electromagnetic spectrum with THz gap

(Source: Rogalskii, et al. 2011)

Therefore, these waves have widespread applications in medicine, T-ray imaging, microelectronics, agriculture, forensic science and many other emerging fields. Although there are many techniques for generating THz radiation such as femtosecond lasers, synchrotron light, backward wave oscillators, etc., there is still lack of powerful, low-cost, continuous-wave, compact, portable room temperature, solid-state terahertz sources.

1.2. Application Areas of Terahertz Radiation

The terahertz regime lies between the microwaves and infrared region; therefore, it is a kind of bridge between these two regimes. Due to its position in the electromagnetic spectrum, it provides extremely useful application in different fields. Hence, terahertz technology is an extremely attractive research field. Because of this, recent developments in terahertz system technology are rapidly growing. These technology developments can be used in many applications areas such as T-ray imaging, medical diagnostics, material characterization etc. Here, I will introduce some of these application areas.

Terahertz imaging: A wide variety of techniques is available for imaging applications. Many of these techniques such as x-ray backscatter and millimeter wave can be used, but imaging with these methods has some drawbacks. For instance, x-ray backscatter uses ionizing radiation, both technologies are likely to provoke a debate on

the privacy issue, and plastic and ceramic materials are hard to being distinguished in backscatter x-ray technique, as there is little contrast between the body and these materials. On the other hand, there is still no technique, which is capable of carrying out a chemical or structural analysis of suspect objects. Otherwise, terahertz radiation has its own advantages. One of the most important reason for using terahertz radiation for imaging application is that it is non-ionizing radiation thus is not expected to damage tissues and DNA, and only triggers vibrational and rotational states of molecules while leaving the electronic states unchanged. Therefore, terahertz radiation is much safer than x-rays due to that it is one million times weaker than x-rays. This radiation has also the ability of detecting differences in water content and density of tissues. Because of this important property, it can be used for effective detection of epithelial cancer with a safer and less invasive or painful method. Some of the applications of terahertz imaging in security inspections, medical diagnosis and quality control can be seen in Figure 1.2.

Moreover using terahertz waves provide high-resolution 3D imaging since extremely short femtosecond pulses are used in pulsed terahertz techniques, which are, enable 3D imaging. Therefore, some frequencies in this part of the electromagnetic spectrum can be used for 3D imaging of teeth and may be more accurate and safer than conventional X-ray imaging in dentistry.

Security: Terahertz radiations can penetrate through many materials such as plastics, packaging material like cardboard, fabrics, human tissues etc., so these kinds of materials leave a spectral fingerprint when terahertz radiation passes through them. Figure 1.3 represents the optical properties of condensed matter in the THz band. Hence, these waves are good source for applications in surveillance such as security screening, to uncover concealed weapon on a person. On the other hand, since terahertz radiations are being targeted to a very specific range of materials or objects, passive detection by terahertz waves avoid the bodily concerns of other detection.

Scientific use: Controlling chemical reaction in chemistry and biology is a significant problem, thus it is essential that the energy inserted to a molecular system should be channeled into specific mode to control the system with high precision. Terahertz radiation has the ability of imaging the changes in complex molecular interactions because of its sensitiveness to changes in the collective modes of a system. In addition, biological molecules have an important feature regarding their relation with water. For instance, protein molecules require an aqueous environment to function and

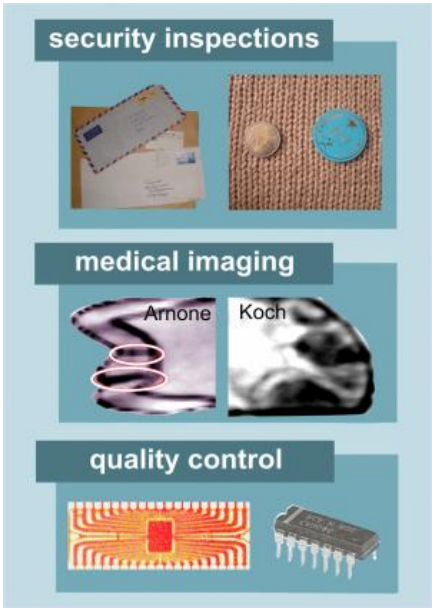

Figure 1.2. Applications of terahertz imaging in security inspections, medical diagnosis and industrial quality control (Source: www2.fkf.mpg.de)

different interfaces such as air/water, water/solid or water membrane demonstrate different characterizations such as density, pH. Hence, for this purpose terahertz spectroscopy can be used because this spectroscopy presents different signatures of biological systems compared with bulk liquid water.

Material Type	**Optical Property**
Liquid water	High absorption ($\alpha \approx 250$ cm -1 at 1 THz)
Metal	High reflectivity (> 99.5 % at 1 THz)
Plastic	Low absorption ($\alpha < 0.5$ cm -1 at 1 THz)
	Low refractive index ($n \approx 1.5$)
Semiconductor	Low absorption ($\alpha < 1$ cm -1 at 1 THz)
	High refractive index (n 3-4)

Figure 1.3. Optical properties of condensed matter in the THz band

THz spectral regime provides information about equilibrium measurements and dynamical processes of inorganic and organic molecules since their phonon modes lie in terahertz region of the electromagnetic spectrum.

Communication: Despite the fact that terahertz radiations are not penetrate through atmosphere, some systems have been developed to communicate with terahertz waves. Some advantages such as small antenna sized and large information bandwidth

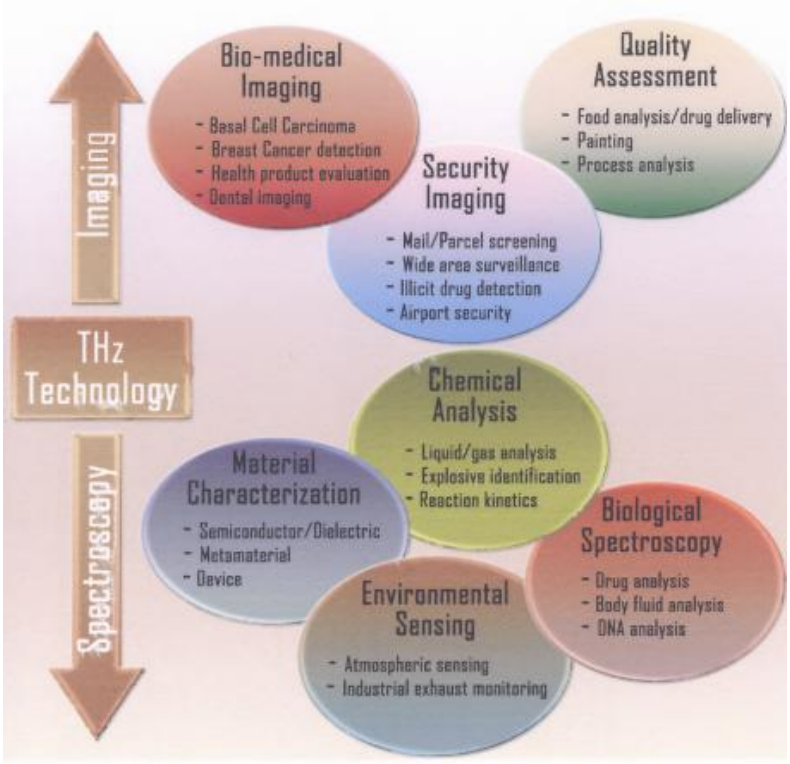

Figure 1.4. Application of terahertz radiation
(Source: Bandyopadhyaym 2006)

can be achieved using terahertz carriers in secure communications. Terahertz radiation can penetrate through aerosols much greater than IR and optical wavelengths, so, terahertz signal are more useful for communications system in the stratosphere. Therefore, this regime of electromagnetic spectrum provides applications exist in high-altitude where water vapor causes signal absorption: aircraft to satellite, or satellite to satellite.

1.3. Terahertz Generation

Since there are many application areas of terahertz radiation, I would like to introduce most commonly used terahertz sources. These, sources can be categorized as incoherent thermal sources, broadband-pulsed techniques or narrowband continues-wave techniques.

Broadband THz Sources: There are various sources for generating terahertz radiation such as photocarrier acceleration in photoconducting antennas, second-order non-linear effects in electro-optic crystal plasma oscillations and electronic non-linear transmission lines. However, all these sources have very low conversion efficiency and because of this, average THz beam powers are in the range of nano-to microwatt rage, while the average power of the femtosecond optical source is in the region of 1 W.

The most common techniques for generating broadband-pulsed terahertz radiation are photoconduction and optical reflection approaches. The former one uses photoconductors at high-speed as transient current source to radiate antennas. Generally, photoconductors consist of high resistivity GaAs, InO and radiation damaged silicon wafers. The physical picture of THz generation using photoconductive antennas based on ultrafast laser pulse, which creates electron-hole pairs in the photoconductor. The other mechanism is optical rectification, which is based on the inverse process of the electro-optic effect. Within these techniques, femtosecond laser pulses are also required and in contrast to photoconducting elements, THz radiation comes directly from exciting laser pulse.

Narrowband THz Sources: Generation of narrowband terahertz radiation is very important for spectroscopy and telecommunication applications. Therefore, there have been rapidly growing interests in the development of narrowband sources over the past century. The most common used technique for generation of low-power terahertz radiation is through upconversion of lower-frequency microwave oscillators such as voltage-controlled oscillators and dielectric resonator oscillators. Here, up conversion is generally obtained by a chain of planar GaAs Scottky-diode multipliers. The other most common sources for generation of terahertz radiation are gas lasers. Within type of sources, a low-pressure gas cavity, which leases at the gas molecule's emission-line frequencies is pumped by a carbon dioxide laser. Although these kinds of sources generally require large cavities and kilowatt power supplies, and they are not

continuously tunable, they can provide high output powers about 30 mW. Recently, it has been showed that free-electron gas lasers with energy-recovering linear accelerators are good candidate to obtain extremely high power THz emissions. Working principle of free electron gas lasers are based on using a beam of high-velocity bunches of electrons propagating in a vacuum through a strong, spatially varying magnetic field. Furthermore, many optical techniques have been developed to generate narrowband terahertz radiation. First attempt to obtain narrowband THz radiation was using non-linear photomixing of two laser sources in 1979s. However, these techniques could not provide high conversion efficiencies. Semiconductor lasers are a promising technique for narrowband THz generation. Yet, this kind of lasers have many limitations including low output power and need for cryogenic cooling to maintain lasing conditions. Quantum cascade lasers (QCLs), discovered in 1994, are semiconductor lasers. QCLs are based on a series of coupled quantum wells and these quantum well are constructed by molecular beam epitaxy technique. QCLs have coupled quantum wells (Figure 1.5), which are described by nanometer thick layers of GaAs, sandwiched between potential barriers of AlGaAs as seen in Figure 1.5. In a quantum cascade laser, there is one injector and one active region. While population inversion exists and electron transition to lower level occurs and generating waves at a specific wavelength in the active region. After that, the electrons tunnel between the quantum well and then the injector region provides coupling of them to the higher energy level in the active region of the subsequent repeat units. The quantum cascade lasers can be used for generating terahertz radiation in the infrared region of electromagnetic spectrum, however generating long wavelength of terahertz radiation with these laser are still very significant problem.

As I mentioned above, while electromagnetic waves in this frequency region (0.1 to 10 THz) have many beneficial applications such as imaging, sensing and spectroscopy (Tonouchi, et al. 2007), many terahertz sources have own disadvantages for practical applications; therefore, there is a great interest to find high power, low cost and tunable terahertz radiation sources.

So, the research has gone towards the novel THz sources, which include technology of high temperature superconductors (HTSs). The most significant reason making HTSs suitable candidate for the generation of THz radiation is their layered structure which makes possible the propagation of electromagnetic wave by Josephson

plasma oscillations and the frequency of the Josephson plasma is in the THz ranges (Tachiki, et al. 1994).

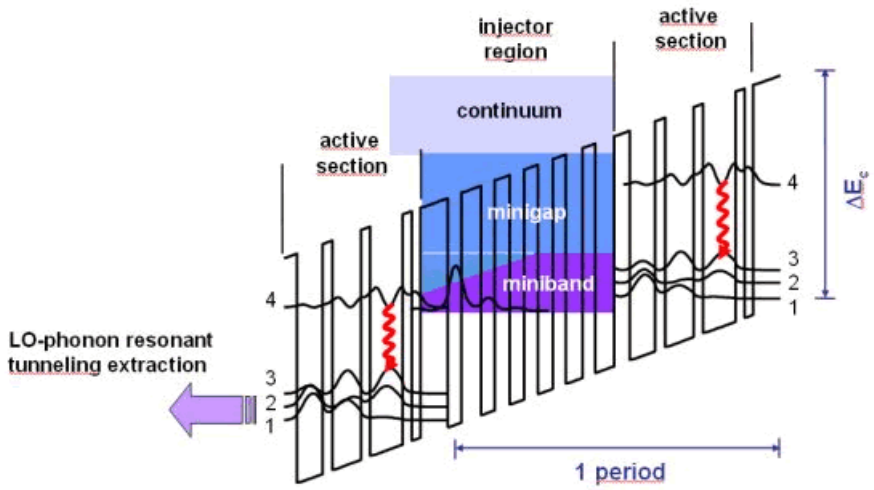

Figure 1.5. Conduction band structure of THz quantum cascade lasers (Source: http://www.wsi.tum.de)

Furthermore, the stacks of IJJs in Bi2212 can be used as voltage-frequency converter (Josephson 1962). After many studies, in 2007, a scientific breakthrough is accomplished. Ozyuzer et al obtained continuous, coherent and monochromatic electromagnetic terahertz radiation from rectangular mesa-shaped sample of the high temperature superconductor Bi2212, in which electromagnetic cavity resonance synchronizes almost all of the IJJ (Ozyuzer, et al. 2007). The details of generation of terahertz waves from HTS superconductor Bi2212 will be explained in Chapter 2.

1.4. THz Generation from HTS Superconductor $Bi_2Sr_2CaCu_2O_{8+d}$

Firstly, radiation in the microwave frequency ranges from Josephson junction observed in 1965 by Langenberg et al. (Langenberg, et al. 1965). However, the radiation power that was in the pW range was very small for practical applications. After that many scientific studies has been finished to develop IJJ arrays to obtain coherent radiation (Jain, et al. 1984, Lukens 1990, Barbara, et al. 1999). Jain et al. showed that it is essential that all the junctions should radiate coherently to obtain maximum radiation, which is proportional with the square of the total number of junctions in the arrays

(Jain, et al. 1984). On the other hand, using artificial junctions and conventional superconductors for terahertz emission is challenging since artificial junctions have different parameters and conventional superconductors have energy gap limitation so that provide radiation in the gigahertz range.

1992, Kleiner et al. showed that layered high temperature superconductors including Bi2212 presents intrinsic Josephson effects that is the basic idea of terahertz generation (Kleiner, et al. 1992). After this breakthrough, a new route opened to develop electromagnetic sources in the terahertz range. Because, large energy gap of high temperature superconductors provides high Josephson frequency in the terahertz range for practical applications of this spectral region. In addition to that, intrinsic Josephson junctions (IJJs) have much more closer parameters than artificial junctions whose parameters are controlled by dielectric layer different from IJJs whose parameters controlled by their atomic crystal structure. Furthermore, since IJJs are very dense structure such that IJJs are about 1.56 nm along the c-axis, they are convenient to reach super-radiation regime with many junctions on the scale of radiation wavelength. Up to now, many efforts have been devoted to develop the mechanism of terahertz generation; however, the same problem to synchronize oscillations in all junctions remains the same.

High frequency radiation of 0.5 THz with a weak power is obtained from unsynchronized intrinsic junctions (Batov, et al. 2006). Many studies have been completed to synchronize the junctions to obtain high power of terahertz emission. For instance, Irie et al. applied a magnetic field to induce coherent Josephson vortex flow (Irie, et al. 1998). Madsen et al inserted the Bi2212 in a microwave cavity (Madsen, et al. 2004). Wang et al used a shunting element parallel to small sized stacks (Wang, et al. 2000). Kume et al proposed excitation of Josephson plasma oscillations by heavy quasiparticle injection (Kume, et al 1999) and Krasnov et al. investigated the simulated emission due to quantum cascade processes (Krasnov 2006). The strategy perhaps investigated the generation of collective Josephson oscillations due to the lattice of moving Josephson vortices, which are exciting electromagnetic cavity resonances inside the stack (Kadowaki, et al. 2006, Bae, et al. 2007). to obtain high power oscillations which are incudes by the moving lattice. The moving lattice have to be in phase in different layers that is occurred only if the moving lattice is generally rectangular. Yet, this kind of rectangular lattices are unstable in most parameters (Koshelev and Aranson

2001). Namely, the vortex-vortex interaction supports the triangular lattice, which produces only weak and noncoherent radiation.

Bulaevskii et al. demonstrated that mesa with small lateral size and a large number of junctions (approximately 104) without applied magnetic field can be used for high power terahertz radiation (Bulaevskii and Koshelev 2007). In addition, they proposed that an electromagnetic field produced by oscillations themselves can be used to synchronized oscillations in different junctions to obtain high power radiation. However it is very difficult technologically to fabricate such a mesa with a large number of identical junctions. In 2007, Ozyuzer et al showed that rectangular mesa structures from intrinsic Josephson junction in Bi2212 single crystal can be used in generating intense, coherent, continues and monochromatic electromagnetic waves in the regime of terahertz frequency. This was an experimental breakthrough since the obtained frequency was as high as 0.85 THz and the radiation power was 0.5 μm different from the previous studies in which the power was one order of magnitude lower than this study. In addition, the radiation power is detected outside the cryostat after travelling the ambient space. Another very important feature of this study is that Ozyuzer et al did not apply any magnetic field to the sample. Simply, a dc current is applied to the system to obtain high power of terahertz radiation, which is also continuous.

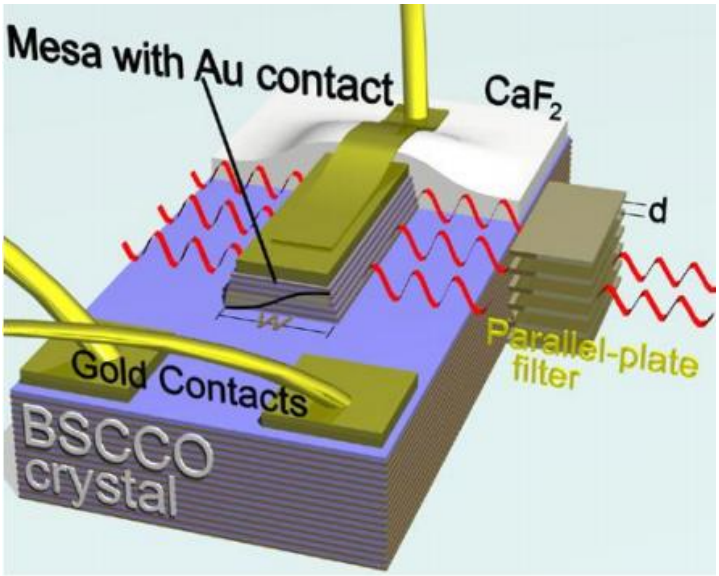

Figure 1.6. Schematic of mesa from Bi2212 crystal for terahertz emission (Source: Ozyuzer, et al. 2007)

In this work, the dimensions of mesa were 300 μm in length, 40-100 μm in width and 1 μm in height as shown in Figure 1.6., which is schematic representation of the system. In this work, an external current is applied through the c-axis of the mesa; current in the resistive state excites a cavity resonance mode of Josephson plasma to obtain terahertz radiation. In this configuration, the standing waves of Josephson plasma converted to the terahertz radiation at the surface of the mesa. Then the electromagnetic wave is emitted in the vacuum space of the mesa.

Kleiner et al. demonstrated that propagation of electromagnetic waves in Josephson plasma modes inside the layered structure of Bi2212 is important for terahertz radiation (Kleiner, et al. 1994). The Josephson plasma mode with highest velocity corresponds to the in-phase mode in which all junctions oscillate in the same mode and the mode with lowest velocity means that the all junction oscillate out-of-phase. Therefore, the terahertz generation can be obtained, only if when the mode is in-phase since the average electric field on the side surface cancels in other modes. When the all junctions oscillate in phase mode, the superposition of the electromagnetic waves result in a macroscopic state in which the radiation power is directly proportional to the square of the number of the junctions. In mesa, when the lateral dimension is smaller than the propagation distance of the Josephson plasma modes, a standing wave pattern is created by the multiple reflections at the side of the mesa. A resonance condition is achieved in such a condition that the Josephson frequency, f_{Jos}, equals the cavity frequency, $f_{cav}= V/(N\Phi_0)$. Here, w is the width of the cavity, V is the voltage applied across the junction stack, Φ_0 is magnetic flux quantum, and N is the number of active junctions in the stack. In addition, the resonance condition leads to that frequency of the radiation can be controlled by the mesa width according to $f \sim 1/w$.

After the breakthrough in 2007, many scientists have studied on THz generation from the layered superconductor Bi2212. Recently, Kadowaki et.al showed one order of magnitude larger power (5 μm) and higher harmonics up to fourth order which correspond to the frequency of 2.5 THz, which can be obtained from the mesa structure from Bi2212 single crystal (Kadowaki, et al. 2008). After that to better understand the mechanism, local temperature properties of emitting mesas and tunability have been observed (Gray, et al. 2009, Kurter, et al. 2009, Wang, et al 2009). Wang et al. observed the electric field distributions in the junctions to get knowledge about confirmation of cavity modes. In this study, this group observed standing electromagnetic waves, which corresponds to the cavity resonances. In addition to that, in the high bias region, they

observed the hot spots, which have higher temperature than the critical temperature and their position can be changed by external current. These hot spots can be used to tune the cavity size and hereby the frequency of the radiation (Wang, et al. 2009). Kurter et al. showed that the back bending of the I-V curves due to the heating is coming from the shape of the $R_{qp}(T)$ (the quasiparticle resistance) in Bi2212. Therefore, in order to find the mesa temperatures along the I-V curves, the V/I and the $R_{qp}(T)$ values are compared and they obtained disappearance of backbending above 60 K (Kurter, et al. 2009). Kurter et al. also showed that the high and sharp peaks in the conductance of intrinsic Josephson junctions in Bi2212 mesas are a result of heating in spite of the fact that they were regarding as superconducting energy gap (Kurter, et al. 2010). Tsujimoto et al. have been used various mesa shaped radiating structures from Bi2212 single crystal to better understand the mechanism. They obtained the frequency spectrum, which exhibited higher integral harmonics of the fundamental f1 and despite of the fact that heating effects obviously changes the I-V characteristics, they do not greatly affect the two necessary radiation conditions. They proposed that the radiation condition should be satisfied when $f_1 > f_p$, here fp is the Josephson plasma frequency (Tsujimoto, et al. 2010). In 2011, Yamaki et al. demonstrated that intense electromagnetic wave generation from rectangular shape mesa structure. The power of radiation was one order of magnitude higher than the previous studies and the power was as high as 30 μm. In addition, the relation between temperature and radiation power were studied in both reversible and irreversible type radiations, suggesting that a non-equilibrium thermodynamic state may be realized through the dc input current (Yamaki, et al. 2011). The tunability of terahertz radiation is found up to 12 % by changing the temperature and bias voltage and this concept is important for design of terahertz devices from the stack of intrinsic Josephson junctions (Benseman, et al. 2011). The effects of electrode thickness are studied by Kakeya et al. They showed that electrode thickness smaller than 100 nm may help excite the Josephson plasma oscillation because of the poor heat flow through the electrode. Moreover, Kakeya et al. proposed that the local temperature increase is the base of the synchronization of the phase kink to obtain radiation in the terahertz region (Kakeya, et al. 2012). Then, Tsujimoto showed that terahertz radiation can be used as a source for imaging applications. They have used a razor blade and Japanese coin inside a brownish paper and managed to image them by terahertz radiation (Tsujimoto, et al. 2012). After that, Benseman et al. obtained 600-microwatt

terahertz radiation by synchronizing three mesa structures at the same time (Benseman, et al. Preprint).

In conclusion, it is revealed that ac Josephson effect is base of the mechanism of terahertz radiation and the cavity resonance is needed to obtain a stronger radiation, despite of the fact that both are working together while radiating.

1.5. Terahertz Detection

The detection of terahertz radiation is vitally important as generation of the waves in the terahertz region of electromagnetic spectrum. Due to the low output power and relatively high levels of thermal background radiation require highly sensitive detectors in this range. So a various kind of detectors technology is developed to measure broad and narrow band signals in this spectral regime. Generally, for broadband detection, the most common used detectors are direct detectors, which are based on thermal absorption. Whereas narrowband detection in THz-TDS systems require coherent detectors and the most common techniques rely on ultrafast laser sources. Now I will illustrate most common used detectors for terahertz sensing applications.

Among many coherent detection techniques, electro-optic (EO) sampling, photoconductive switching, photomixing and heterodyne detection are most commonly used to detect terahertz waves. By free electron-optic (EO) sampling, the actual electric field of broadband terahertz pulses are measured. The actual electric field is detected by utilizing Pockels effects, which is closely related to optical rectification. Another method of measuring broadband terahertz pulses in the time domain is detecting with PC antenna. When there is no bias field, a THz field induces a current in the photoconductive gap when optical probe pulse injects photocurrents. The induced photocurrent is proportional to the THz field amplitude Measuring the photocurrent provides mapping the terahertz pulse shape in the time domain while varying the time delay between the THz pulse and optical probe. Photomixing, another type of measuring CW (continues wave) THz radiation, is based on exploiting photoconductive switching. In this method, the photocurrent displays sinusoidal dependence on the relative phase. The detection of terahertz radiation with heterodyne detector utilizes a

nonlinear device, which is known as mixer. In this type of detection, Schottky diodes are used as mixers.

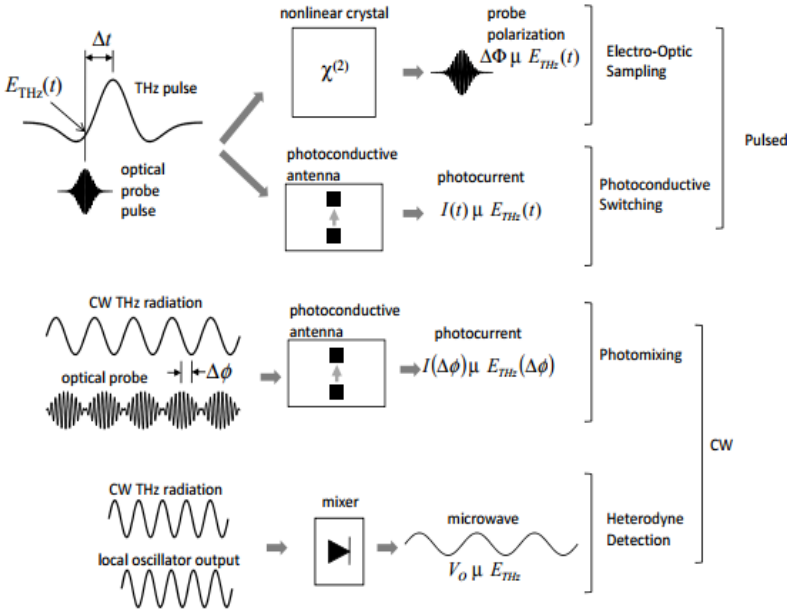

Figure 1.7. Coherent detection of terahertz radiation
(Source: Principles of Terahertz Science and Technology)

The mixer here stands for producing an output signal at the difference frequency called the 'intermediate frequency'. Here, the amplitude of the output signal of radiation is proportional to the THz amplitude. Heterodyne detection technique is generally used to detect CW incoherent terahertz radiation as different from the optical techniques.

Among so many incoherent detector types to sense terahertz radiation, pyroelectric device, bolometers and Golay cell are most commonly used thermal sensors. Basically, all these types of devices have a radiation absorber attached to a heat sink and a thermometer is used to measure the temperature difference in the absorber. These thermal detectors are classified into by its specific scheme, which is used to measure the temperature difference.

Generally, pyroelectric detectors have been offered for terahertz applications, which do not require high sensitivity. Pyroelectric materials including TGS or Lithium Tantalate shows a large spontaneous electrical polarization and this kind of detectors can only sense AC signals. In addition, pyroelectric detectors have the ability of operating at room temperature. Gallium doped Germanium photoconductive detectors

are another type of sensing devices and have photoconductive response out to wavelengths longer than any other combination of elements. When there is no stress available, the cut-off wavelength is about 120 µm whereas when stress is applied to the detector crystal the number increases approximately 200 µm.

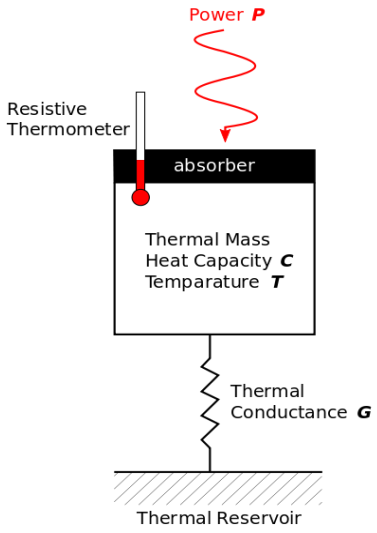

Figure 1.8. Bolometer detector
(Source: www.wikipedia.com)

Bolometer detector, is a radiant detector, was invented by Samuel Pierpont Langley in 1878. This kind of thermal detector is very sensitive to differences in temperature. Thermal detectors have the ability to convert the incident radiation to heat then the active element is used to response to the heat, as a result of this, the heat input causes in some measurable physical property of the device. The schematic representation of the bolometer detector can be seen in Figure 1.8.

Golay cell: Golay cell is invented by M. J. E. Golay in 1947. A Golay cell detector is a room temperature detector, which is relied on differences in volume or pressure of an encapsulated gas with temperature. Basically, when the incident electromagnetic radiation reaches to this type of detector, the volume change is measured by the deflection of the incident lights. In addition, Golay cell is a metal cylinder, which has two ends; one is a blackened metal plate and the other is a flexible metalized diaphragm. To measure the volume or pressure differences, this cell is filled with an inert gas.

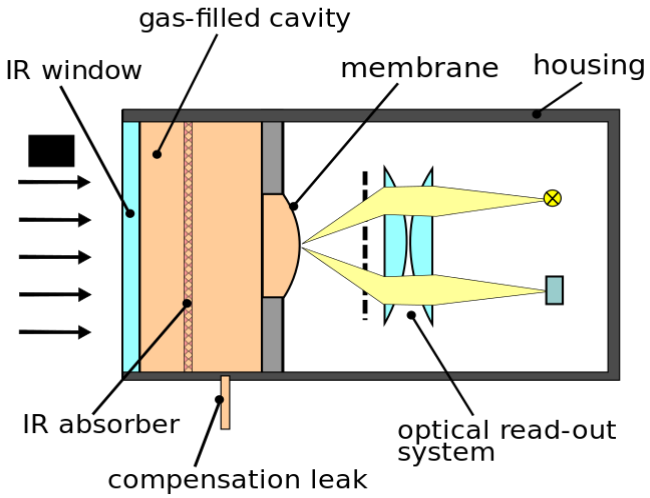

Figure 1.9. Golay cell

(Source: www.wikipedia.com)

When an electromagnetic radiation is absorbed by blackened metal plate then the inert gas heats and the heated gas make some pressure differences and thereby expands the diaphragm. Finally, the incident flux is measured by the reflection of light from the motion of diaphragm. The schematic representation of Golay cell can be seen above in Figure 1.9 Golay cell has some advantages and disadvantages. For instance, this kind of cell responds to all radiation if spectral sensitivity is tuned by selecting the front window material appropriately and cooling is not required for operation. However, the membrane used is very fragile and since working principle of Golay cell is based on thermal response, their maximum speed of useful operation is 20 Hz.

In order to obtain terahertz measurements of our fabricated mesas, we have used the Golay cell since it has many advantages when we compared other terahertz detectors. The detail experimental set up will be given in Chapter 3.

CHAPTER 2

THEORETICAL BACKGROUND

2.1. Introduction

Superconductivity was discovered by Kimberling Ones in 1911 during his experiment on measuring the electrical resistance of mercury at low temperatures. After that, great scientists such as Einstein, Landau and Heisenberg completed many scientific studies. Then Bardeen, Cooper and Schrieffer introduced the BCS theory of superconductivity in 1957. Basically, the BCS theory refers to the interaction of a gas of conducting electrons with phonons. It is well known that two electrons in vacuum repel each other due to the Coulomb attraction force. However, if these two electrons are in a superconductor material, they will attract each other below the critical temperature Tc. After the introduction of BCS theory, the new type of superconductor materials, (organic superconductors and heavy fermions) were discovered in 1979. Exciting news came after the discovery of new type of superconductors; copper oxides (cuprates). At that time, it was very astonishing that the cuprates were very bad conductors. The discovery of cuprates stimulated the studies on both experimental and theoretical fields. After that, many scientific studies revealed that the characteristics of high temperature superconductors show some different properties which cannot explain by BCS theory. For instance, the BCS isotope effect, an important theory that provide a relationship between the critical temperature and the isotope mass of most of conventional superconductors, cannot seen in cuprates. To sum up, phonon-electron interaction with the assistance of spin fluctuations is the only theory that is known today and the strength of phonon-electron interactions vary from materials to materials. While the strength is very weak in metals, cuprates show moderately strong strength. Furthermore, in metallic superconductors, the wave functions coupling provides long-range phase coherence; on the other hand, the phase coherence is established in high-T_c superconductors as well as organic compounds and heavy fermions by magnetic fluctuations.

2.2. A Brief History of Superconductivity

In this section, brief history of superconductivity will be summarized to better understand the mechanism of high-T_c superconductor materials. As mentioned above, superconductivity was introduced by the Dutch physicist H. Kamerlingh Onnes in 1911. In his studies, it is discovered that the dc resistivity of mercury drops to zero below the temperature of 4.2 K.

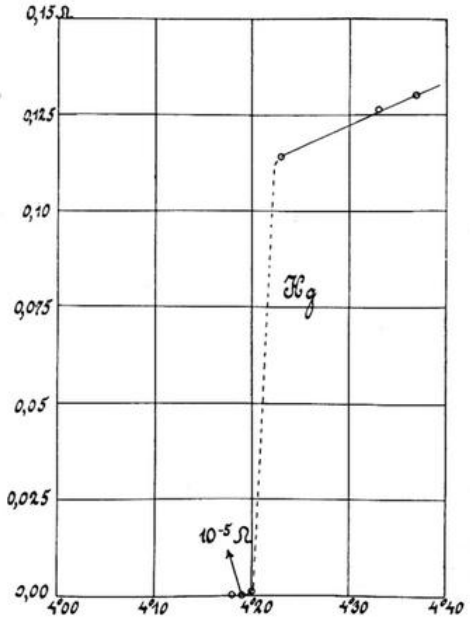

Figure 2.1. The first introduce of superconductivity
(Source: Ones 1911)

The other decisive discovery achieved by W. Meissner and R. Ochsenfeld in 1933. These two great scientists introduced the perfect diamagnetism in superconductor materials. They revealed that the magnetic flux inside a superconducting material is expelled when it is cooled below the transition temperature in weak magnetic fields. In 1934, two-fluid model that provides a useful point of view to understand the thermal properties of superconductors was discovered by C.J. Gorter and H.B. G. Casimir. The other decisive phenomenon was existence of vortices in superconductors in external magnetic fields discovered by L. V. Shubnikov and his co-workers in 1937. Then, in 1950, the isotope effect and Ginzburg-Landau theory played an important role to better understand the superconductivity phenomena. In 1957, J. Bardeen, L. Cooper, and R. Schrieffer were first proposed the microscopic theory of superconductivity that is well

known as BCS theory in metals. In 1962, another scientific important achievement came; B. D. Josephson theoretically predicted quantum mechanical tunneling of copper pairs through a thin insulator layer with thickness of few nanometers. This phenomenon has an important impact on superconducting applications. In 1986, the discovery of high-Tc superconductivity in cuprates stimulated the researches on superconductivity. This significant discovery was made by J. G. Bednorz and K. A. Muller. Soon after, in 1987, Anderson predicted a model of superconductivity in cuprates and this model was about the pairing mechanism and phase coherence difference. Then, in 1990. A. S. Davydov proposed a decisive theory related to the concept of strong electron-phonon coupling. The theory makes use of the idea of bisolitons, or electron (or hole) pairs, which are coupled in a single state owning to the existence of the local deformation of the -O-Cu-O-Cu- chain in CuO_2 planes. At the beginning of 1900s, Anderson predicted that the pairing mechanism and mechanism for establishment of coherence differ from each other. Afterwards, in 2001, it is understood that the tunneling spectra of Bi2212 single crystal resulted from condensation of solitonlike excitations that form the copper pairs.

2.3. Superconducting Materials

After Ones's crucial observation, thousands of new superconductor materials were introduced. The superconducting materials can be distinguish by their properties as follows; metals, binary alloys and compounds, Chevrel phases, semiconductors, organic quasi-one-dimensional superconductors, heavy fermions, oxides, high-Tc superconductors and others.

The story about high-Tc superconductor cuprates began in 1989 by the discovery of ceramic superconductor La-Ba-Cu-O at about 30 K. After that new highest transition temperature at about 93 K came from the studies on YBCO by M. K. Wu and P.W. Chu. Then, Bi- and Ti based superconductor cuprates with transition temperature of 110 and 125 K respectively discovered and finally Hg-based cuprates with T_c of 135 K introduced in 1993. Figure 2.2 shows the timeline of discovery of superconducting materials. Here, all these cuprates are hole-doped and the only electron-doped one is (Nd,Pr,Sm) CeCuO introduced in 1989 with relatively low T_c about 24 K.

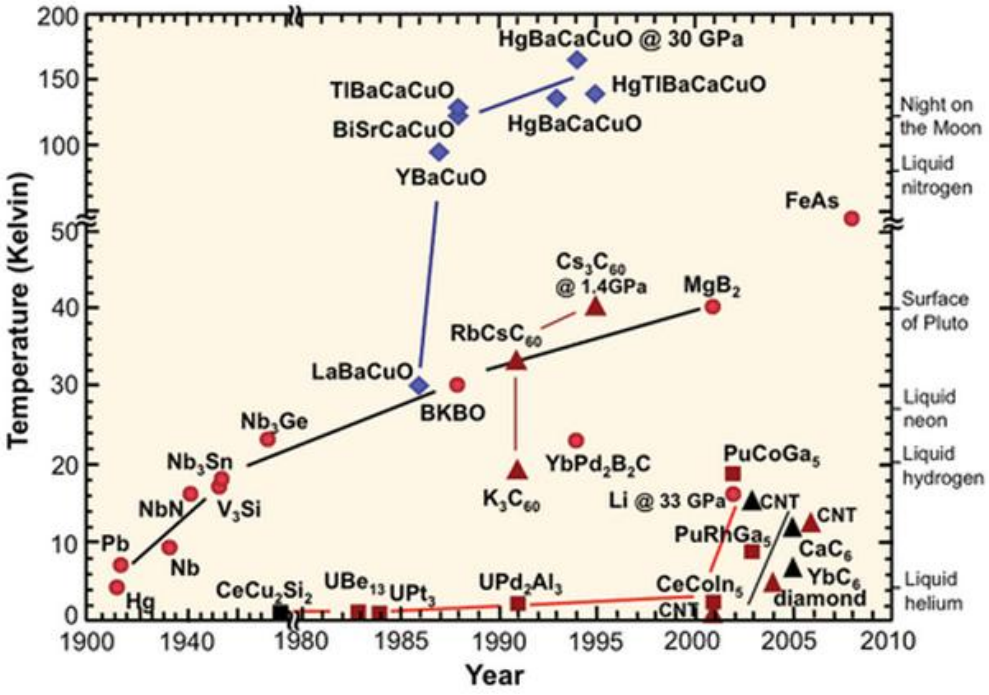

Figure 2.2. The timeline of discovery of superconducting materials

(Source: Image courtesy of Department of Energy - Basic Energy Sciences)

2.4. Characteristic Properties of Superconductors

Purpose of the present section is to better understand the behavior of superconductor materials at low temperatures and see that below a transition temperature these superconductor materials show abrupt change in their thermal and electrodynamics properties. It is a well-known phenomenon that the resistivity of normal metals decreases steadily and then reaches its constant value of ρ_o. However, the resistivity of superconductor materials dropped significantly to extremely small values. Typically, the resistance drops abruptly to several orders of magnitude at the transition temperature and it is not possible to prove that the resistance is zero below the critical temperature. Therefore, the most useful way to investigate the upper limit of the resistance for a superconducting material is detect the magnetic field generated by the super current. For example, an upper limit for low temperature superconductors is determined as 3.6×10^{-23} Ω.cm (Quinn, et al. 1962). Hence, the super current can be regarded as endless current for practical applications.

Transition mechanism for normal and superconducting metals are very simple while chemically complex materials such as Bi-, Ti-, and Hg-based cuprate

superconductors show several superconducting phases in their resistivity versus temperature graphs. For instance, two steps correspond to two different superconducting transition phases. Typically, single-phase high temperature materials show less sharp superconducting transition than metallic low temperature superconductors and the transition width for single-phase high-T_c superconductors are generally approximately 1K.

The other important property of superconducting state is perfect diamagnetism. When a superconductor is cooled below the critical temperature and then applied a magnetic field, due to the time dependence magnetic field, the permanent screening currents are induced in the surface of the superconductor. Then an opposite flux density, opposite to the applied field, is generated by the currents. Because of this, the magnetic field inside the superconductor material is expelled. This is similar mechanism to that of a perfect conductor. In the second case, while the material is being cooled, at the same time a magnetic field is applied. Once the temperature of the sample reaches to the transition temperature, suddenly the magnetic field is expelled from the interior of the superconductor material. This decisive phenomenon is also called as Meissner effect. The Figure 2.3. illustrates the schematic representation of the steps for perfect conductor (a) and superconductor material (b). Here, there is a remarkable point that the perfect conductivity is not sufficient to explain the Meissner effect. Due to the limited value of the critical current density, the screening currents find the opportunity of flowing in a layer flow of finite thickness and the magnetic field applied penetrate through the thin layer and when the applied field exceeds certain magnetic field value then the superconducting state turns into normal state. Furthermore, these transition temperature and critical magnetic field values strongly related to the superconductor material's crystal structure.

2.5. The BCS Mechanism

In this section, the microscopic theory of superconductivity in conventional superconductors, which is also well known as BCS theory will be briefly explained. Great scientists H. Fröhlich and J. Bardeen introduced that electrons can interact with each other by lattice vibrations, which are also called as phonons.

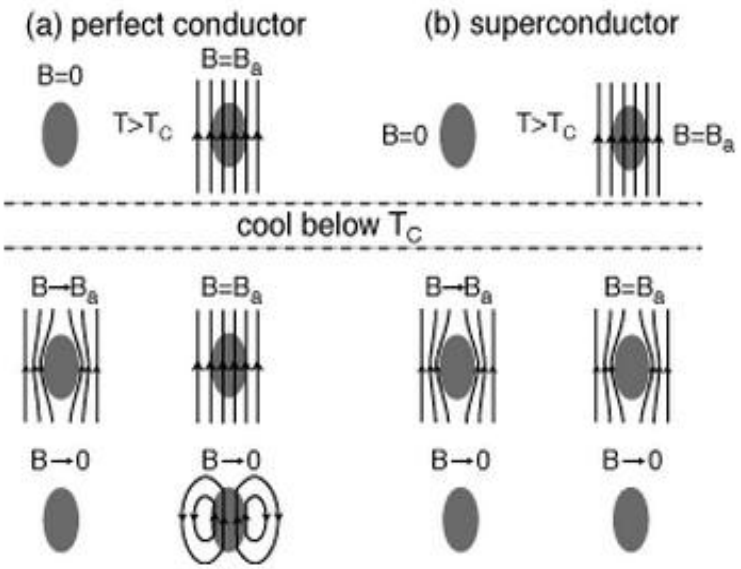

Figure 2.3. Meissner effect
(Source: http://users-phys.au.dk)

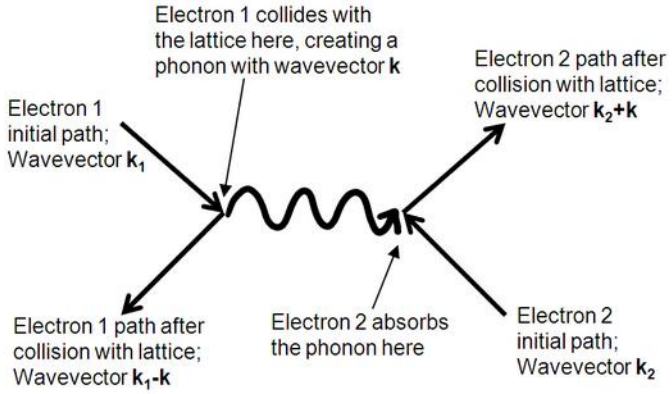

Figure 2.4. A model of Cooper pair attraction
(Source: http://hoffman.physics.harvard.edu)

It is known that the basic mechanism of electrical resistance in a metal is the interaction of electrons and lattice. This basic interaction also causes superconductivity under certain conditions and results in zero resistance. This is the reason that some pure metals such as silver, gold do not show superconductivity; however, such metals show a resistance at near absolute zero. This Figure 2.4 schematically represents the electron-phonon interaction. The interaction between phonon and electron can be summarized as follows; when electrons move in a periodic lattice, they tend to disturb the lattice due to

the attraction between positively charged lattice and negatively charged electrons. When the distortion continues for a short period, the second electron will fell it and then will be affected by it. Under some conditions, this provides a weak indirect interaction between these two electrons. Here, the bounded electrons are called as Cooper pair that has opposite momenta and spins. The cooper pairs behave like a boson that means they can be available in the same quantum state and they have a lower level of energy and leave an energy gap above them approximately .001 eV which blocks the kind of collision interactions that lead to ordinary resistivity. When thermal energy is less than the band gap, the material shows superconductivity, i.e. zero resistivity. This important opinion led to Bardeen, Cooper, and Schrieffer to receive the Nobel Prize in 1972.

2.6. Type I and Type II Superconductors

Superconducting materials have the ability of being in the normal state or superconducting state according to the magnetic field which they are exposed. When the

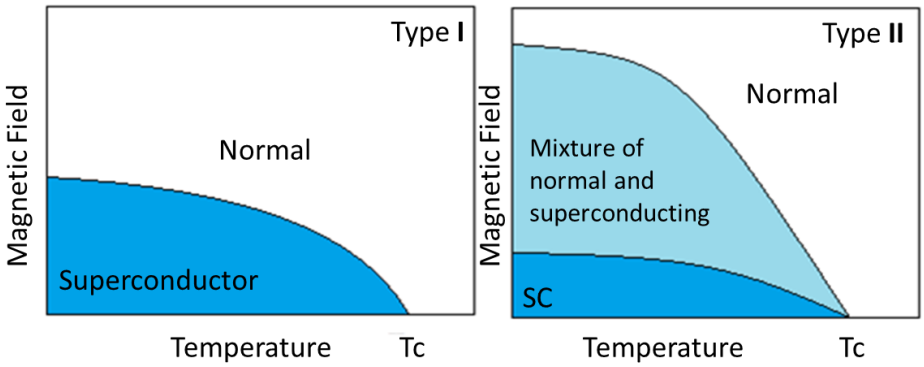

Figure 2.5. Type 1 and Type 2 superconductors

applied field exceeds the critical magnetic field value H_c or H_{c1} that differs from material to material, the Meissner effect destroys, i.e. magnetic flux have the opportunity of penetration through the superconducting material. At the lower value of magnetic field, the Meissner state dominates. However when the magnetic field increases, there will be two different situations that can be classified into as follows and these two will provide us to sort all known superconductors. The magnetic property of these two types of superconductors can be seen in the Figure 2.5.

Type I Superconductors: The Type I category of superconductors is also called as soft superconductors were discovered firstly and require the coldest temperatures to become superconductor. In these kind of superconductors, when the applied magnetic field value pass a critical value of H_c, superconductivity abruptly vanishes via first order transition. Pure metals such as aluminium, leas and mercury exhibits such kind of behaviour. Besides, the transition from normal state to superconductor state and perfect diamagnetism is very sharp and they require extremely low temperatures to slow down the molecular vibrations to facilitate unimpeded electron with respect to the BCS theory. Furthermore, the magnetic field flux penetrates through the sample in the form of continuous lamina in these types of superconducting materials. The lamina, which has a relative thickness depend on temperature and applied field, is altering normal and superconducting layers, parallel to the applied field. There are some constraints to use these structures for applications; there is no flux in a Meissner-like state, whereas the normal states have a magnetic flux density corresponding to the critical fields, $B_c=\mu_0 H_c$ and the relative thickness of normal and superconducting lamina can be determined by considering this fact and flux quantization.

Type II superconductors: The new family of superconductors were introduced by W. de Haas and J. Voogd in 1930 by recognising two distinct critical magnetic fields (known H_{c1} and H_{c2}). These types of superconductors, also known as hard superconductors, allow the applied field to partial penetration at a critical field H_{c1}. In addition, here, the penetration occurs in a form of quantized vortices, which is also well known as Abrikosov vortices. Type 2 superconductors include metallic compounds and alloys except; vanadium, technetium and niobium and the perovskites belong to this group of superconductors. They have higher transition temperature from superconducting state to normal state, however, the mechanism of this type of superconductivity has not fully understood. It is widely believed that this mechanism is related to the crystal structure of superconductor materials. Yet, recent research proposed that it is about the holes of hypocharged oxygen in the charge reservoirs. While some theoretical calculations predict a upper limit for the layered cuprates (Vladimir, et al. 1997), others state that there is no limit. In the both theory, there are still more-synergetic compounds await discovery.

In Type II superconductor materials, the magnetic fluxes have the ability of penetration through tiny, precisely quantized units of flux, $\Phi_0 = h/2e = 2.067833758$

$(46)\times10^{-15}$ Wb and here h: Planck's constant, e: magnitude of electronic charge. Moreover, the density of flux lines increases when the applied magnetic field increases.

2.6.1. Type II Superconductor: Bi2212

In1986, the first high-T_c superconducting element was introduced by Bednorz and Muller at IBM Zurich Research Laboratory (Bednorz, et al. 1986). Certainly, the discovery was a revolution for superconducting applications since it was proved that superconductivity can occur at higher temperature than 30 K and also can be seen in very bad conductors.

If a superconductor has CuO_2 planes, it is said that the superconductor belongs the family of high-T_c superconductors (cuprates) and the antiferromagnetic Mott insulators. Mott insulators are known as the parent compounds of superconducting cuprates and a Mott insulator can be described as a material in which the conductivity vanishes while temperature tends to reach zero on the contrary to that the band theory proposes that it should be metallic. Furthermore, the cuprates is the only superconducting family, which is known as Mott insulator. The crystal structure of cuprates is referred as perovskites. Here perovskites are minerals and have chemical formula as ABX_3 or AB_2X_3. Because of this, the structures have three elements, which are A, B, X with ratio 1:1:1 or 1:2:3. Atoms A stands for metal captions, atoms B and X are non-metal compounds and element X is for oxygen. According to location of atoms, the physical properties of cuprates can be understood and the crystal structure of these superconducting materials shows anisotropy. In conventional superconductors, the coherence length is much longer than the penetration depth, as a result of this there are no significant structural effects. However, this is completely different for high temperature superconductors (cuprates). The high temperature superconducting materials, all of them consist of one or more CuO_2 planes typically have tetragonal crystal structure. Superconductivity in this cuprates occurs in the copper-oxide planes and these copper oxide planes generally separated by Bi, O, Y, Ba, La, etc. atoms. These atoms supplies charge carriers through the copper-oxide planes. Therefore, these atoms generally are known as charge reservoirs. Also in the CuO_2 planes, each copper atom connected to four oxygen ions, which are separated by the thickness of 1.9 ^{o}A. In general, when the CuO_2 layers in a unit cell changes, the critical temperature also

changing, this means that critical temperature of a cuprate is related to the number of copper oxide layer.

Bi2201 and Bi2223 are other groups of cuprates which have CuO_2 planes as 1, 2 and 3 respectively and T_c is increasing with the number of CuO_2 planes.

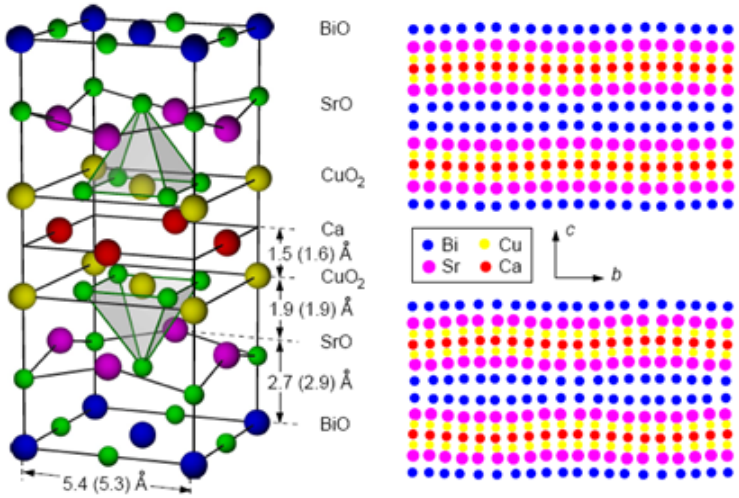

Figure 2.6. Crystal structure of Bi2212 and crystal structure from x-ray diffraction (Source: http://www.phys.ufl.edu)

The Figure 2.6 represents the unit cell of Bi2212 single crystal and the lattice constants are a ≈ b ≈ 5.4 ^{o}A and c ≈ 30.89 ^{o}A. This provides an important property that there is not twining in Bi-based crystal since the lattice constant is a ≈ b. The Figure 2.6 also illustrates that this structure consists of two semiconducting BiO and two insulating SrO layers in addition to that the CuO_2 layers are intercalated by Ca. In addition, in this structure, Bi has +3 valance while Sr has +2. Furthermore, the Bi2212 crystals have a lattice modulation along b axis as 4.76 b.

Bismuth cuprates have some advantages for tunnelling and other measurements, first of all, Bi2212 (Bi2201 or Bi2223) have stable oxygen level at room temperature on the contrary to that YBCO have. Secondly, Bi2212 has very weak bonding between the BiO layers so it is very easy to cleave them from these surfaces. It means that when Bi2212 is cleaved, a fresh and clean BiO surface can be obtained. Different from these advantages, it is generally believed that these samples haven't attained structural perfection as obtained in YBCCO crystals.

2.7. Tunneling Process

To begin with, I strongly believe that the requirements for tunnelling should be briefly explained to better understand the tunnelling mechanism. First of all, a barrier between of the system should be exist to protect electrons from direct transportation and the system energy should be conserved, i.e. in the two electrons tunnelling process, the energy gained by on electron is the same the energy loosed by the other. Thirdly, tunnelling continue through the empty states to keep the Pauli exclusion principle. A bias voltage is applied to the positive side to bring the same level the occupied energy level on one side of the barrier with empty levels on the other to make suitable the tunnelling.

Now, I will mention about three different tunneling processes which are normal-metal-insulator tunneling, normal metal-insulator-superconductor tunneling and, superconductor-insulator-superconductor tunneling.

2.7.1. Normal Metal-Insulator-Normal Metal Tunneling

When we consider two metals, which are isolated by an insulator, the Fermi levels are the same and there is no tunnelling between the energy levels (Figure 2.7 (a)).

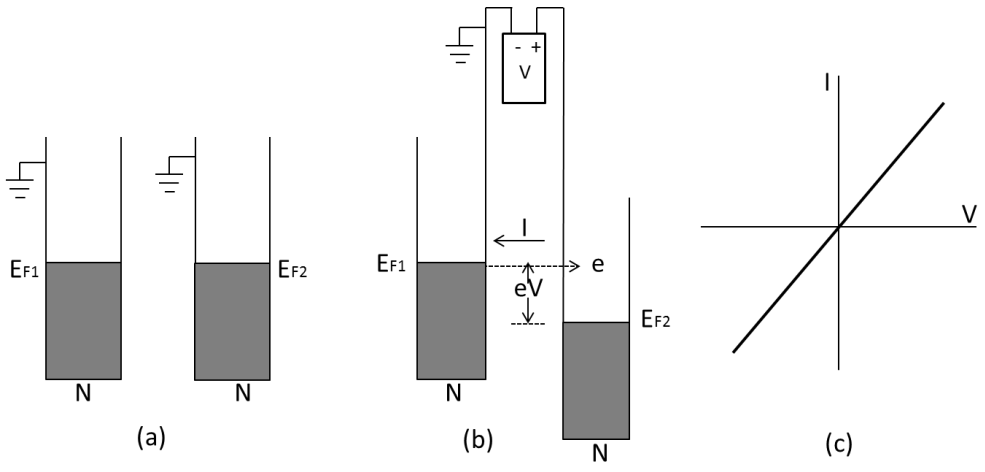

Figure 2.7. Normal metal-insulator-normal metal tunneling

Then, when a positive voltage applied to the one of the metals, resulting in lowering the energy level and causes the tunnelling of electrons from the grounded metal to the

positively biased one (Figure 2.7 (b)). Here, the number of electrons in the empty levels and current, which flows, are related to the bias.

The current- voltage (I-V) curve of normal metal-insulator-normal metal tunnelling can be seen in Figure 2.7 (c). In addition, the magnitude of the tunnelling current is extremely smaller than the current that flows when there is no barrier. Therefore, this is an evidence of the three conditions that presence of barrier, energy conservation and empty target levels.

2.7.2. Normal Metal-Insulator-Superconductor Tunneling

The second case is putting an insulating layer between a superconductor and a normal metal. In this case, the tunnelling occurs through the process as shown in Figure 2.8 Here the three diagrams above represent the semiconductor representation and the three middle diagrams stand for the boson condensation representation. Firstly, when there is no bias, tunnelling cannot occur since there is no way for energy to be conserved by electrons

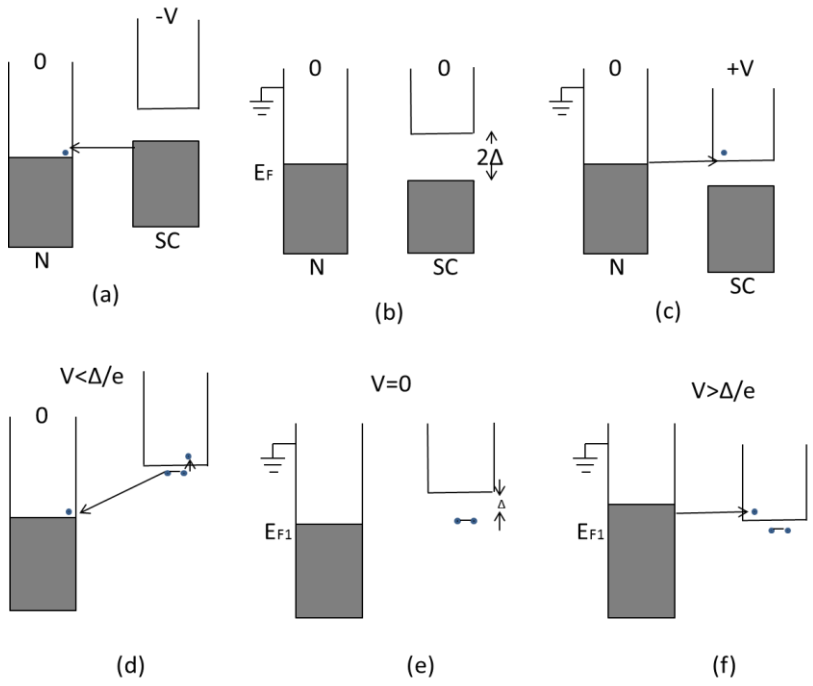

Figure 2.8. Normal metal-insulator-superconductor tunneling

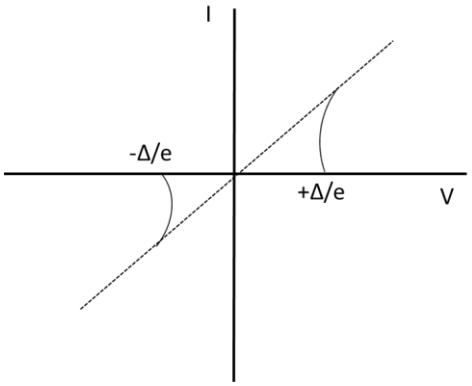

Figure 2.9. I-V characteristics of normal metal-insulator-superconductor tunneling

tunnelling and this is the same for the range $-\Delta/e<V<+\Delta/e$. However, the electrons have the ability of tunnelling through the barrier for a positive bias, $V \geq \Delta/e$. Since Copper pairs do not participate, the scenery looks like each other. However, for a negative bias, $V \leq -\Delta/e$, the interpretation is different for these two cases. In the semiconductor representation, the important thing is that the electron, which is transferred to the conduction band, is taken into as shown in Figure 2.8 (a) and Figure 2.8 (c). Then the transferred electron leaves a hole to create a quasiparticle.

Apart from the semiconductor representation, in the boson condensation picture, one electron of cooper pair jumps to the quasiparticle energy band of the superconductor, and the other down to the top of the normal metal conduction band. Hence, the copper pair breaks up to create a quasiparticle in the superconductor and an electron to the conduction band. This representation can be easily seen in Figure 2.8 (d) and Figure 2.8 (f).

2.7.3. Superconductor-Insulator-Superconductor Tunneling

Our third case is the tunnelling between two identical superconductors. For the range of $-2\Delta/e < V < +2\Delta/e$, an electron has the chance of tunnelling from the superconducting state of one electron to become a quasiparticle in the normal state of the other, which can be seen in the Figure 2.10 (a) and Figure 2.10 (c). Another representation can be seen in Figure 2.10 (d) and Figure 2.10 (f) as the two condensation levels separate and one of the electron jumps up to become a quasiparticle and the other electron jumps down to become a quasiparticle in the other superconductor.

When the bias voltage exceed the range $-2\Delta/e < V < +2\Delta/e$, the current increases and then reaches its normal metal value and it is seen in the Figure 2.11 that the current-voltage graph is anti-symmetric about the point V=0 and it is obvious from the graph that the onset of the tunnelling is $V= \pm 2\Delta/e$. This case is for T=0 and there would be some quasiparticles when the temperature increases and so, some of the tunnelling current will flow for bias voltages below $2\Delta/e$.

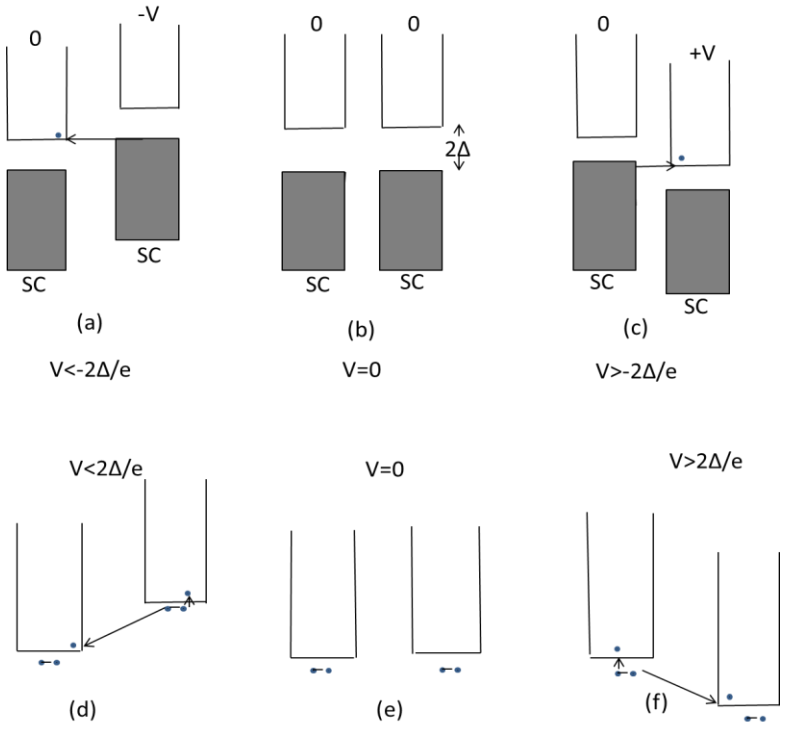

Figure 2.10. Superconductor-insulator-superconductor tunneling

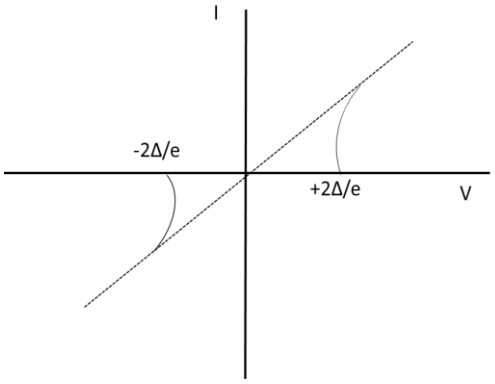

Figure 2.11. I-V characteristics of superconductor-insulator-superconductor tunneling

2.8. Josephson Junction

In 1962, B. D. Josephson suggested that two electrons could tunnel through a thin insulator barrier between two superconductors even though there is no any potential difference. After that, in 1964, an observation about the concept has been made by Anderson and Rowell.

Josephson junction, a junction separates two superconductors, is an active device for superconductor applications. This junction is very weak so that allows these two superconductors wave functions to overlap. In addition, because of the weak junction, the electron can tunnel through the barrier even though there is no applied voltage across it. Unlike quasiparticle tunnelling, copper pair tunnelling does not contain excitations. This means that, if one applies a current source to a junction, then lossless current transport will be achieved until a certain current value. When the current value exceeds the certain value, Copper pairs will not carry the current and some voltage will be developed in the system.

First, we will consider the effect of wave functions that are very close to each other. It is known that when the distance is very large, the pairs in each superconductor can be represented by;

$$\Psi = \left|\Psi(\underset{r}{\rightarrow})\right| exp\left\{i\left[\theta\left(\underset{r}{\rightarrow}\right) - \left(\frac{2E_F}{\hbar}\right)t\right]\right\} \tag{2.1}$$

Here, the phases of these two wave functions are independent. When the distances between superconductors are reduced, the wave functions are able to penetrate through the barrier between them and the energy of the system decreases due to the coupling. When the energy reduced due to the coupling exceeds the thermal energy, the system is locked and Copper pairs pass through the barrier without losing energy. Now let us see that pair tunnelling can also occur when there is a voltage across the junction, so, the coupled Josephson junctions can be described as,

$$i\hbar\frac{\partial\Psi_1}{\partial t} = U_1\Psi_1 + K\Psi_2 \tag{2.2}$$

$$i\hbar\frac{\partial\Psi_2}{\partial t} = U_2\Psi_2 + K\Psi_1 \tag{2.2}$$

The U_1 and U_2 mean the energies of the wave functions for these superconductors and K is the coupling constant. Here coupling constant K is related to the interaction of the two wave functions. When a voltage source applied to the two superconducting sides, then the difference of energy become; U_2-U_1 = e*V. Here it is assumed that the zero energy is the midpoint of the energies U_1 and U_2.

$$i\hbar \frac{\partial \Psi_1}{\partial t} = -e^* \frac{V}{2} \Psi_1 + K\Psi_2 \tag{2.3}$$

$$i\hbar \frac{\partial \Psi_2}{\partial t} = -e^* \frac{V}{2} \Psi_2 + K\Psi_1 \tag{2.4}$$

Expressing the wave functions (2.3) and (2.4) in terms of pair density is convenient, so,

$$\Psi_k = (n_{sk}^*)^{1/2} e^{i\theta_k} \tag{2.5}$$

Here, k is for 1 or 2. When we use the equations (2.3) and (2.4), and then separating the real and imaginary part of the new form and using the phase difference expression $\phi = \theta_2 - \theta_1$, we obtain the following expressions,

$$\frac{\partial n_{s1}^*}{\partial x} = 2/\hbar \text{ K } (n_{s1}^* n_{s2}^*)^{1/2} \sin\phi \tag{2.6}$$

$$\frac{\partial n_{s2}^*}{\partial x} = -2/\hbar \text{ K } (n_{s1}^* n_{s2}^*)^{1/2} \sin\phi \tag{2.7}$$

$$\frac{\partial \theta_1}{\partial t} = -K/\hbar \left(\frac{n_{s2}^*}{n_{s1}^*}\right)^{\frac{1}{2}} \cos\phi + e^* V/2\hbar \tag{2.8}$$

$$\frac{\partial \theta_2}{\partial t} = -K/\hbar \left(\frac{n_{s1}^*}{n_{s2}^*}\right)^{\frac{1}{2}} \cos\phi - e^* V/2\hbar \tag{2.9}$$

From the equations (2.6) and (2.7), it can be obviously seen that the rate of decrease of pair density in one superconductor is the negative of that in the other. Using the comparison with phenomena in a bulk superconductor, the sign of the current density can be determined. The current density J is opposite direction with the grad (θ). In the

Josephson junction, when ϕ is greater than zero, it corresponds to the positive gradient from 1 to 2. So the current density is positive when ϕ is smaller than zero. Because of that the transfer of electrons from 1 to 2 should be exist for this current polarity, then time derivation of ns2* should be positive and therefore, k is negative. Hence, the current density from 2 to 1 obtained as following equation (2.6);

$$J = J_c \sin\phi \tag{2.10}$$

Here, Jc is the critical current density. Moreover, we can evaluate the difference of phases across the junction at any point by subtracting (2.8) from (2.9) and equating ns*1 and ns*2 as;

$$\frac{\partial\phi}{\partial t} = \frac{2e}{\hbar}V \tag{2.11}$$

Here, e* is used as -2e. The equations (2.10) and (2.11) are known as Josephson relations that express electron pairs behavior. When the temperature and the voltage across the Josephson junction are different from zero, there exist a current, which belongs to the quasiparticles.

AC Effects: When dc voltage is applied across the junction, the integration of time evolution of phase results in,

$$\phi = \phi_0 + (2e/\hbar)\,Vt \tag{2.12}$$

If the equation is placed in the (2.10), one can take,

$$I = I_c \sin(\omega_j t + \phi_0) \tag{2.13}$$

This equation above means that there is a ac current at a certain frequency, when a dc voltage applied across the junction, Here the frequency of the oscillations can be expressed by;

$$f_j = \frac{\omega_j}{2\pi} = \left(\frac{1}{2\pi}\right)\frac{2e}{\hbar}V \tag{2.14}$$

The constant part of the equation above is 483.6 × 1012 Hz/V. And also it has been demonstrated that the critical current (I_c) does not depend on frequency. Therefore, when the amplitude of the oscillation changes, the frequency also changes. Moreover, the substantial ac pair currents flow even when the junction voltage exceeds the gap by several times.

2.9. Doping Dependence of Bi2212 Single Crystal

It is well known that the physical properties of high temperature superconductor cuprates are strongly related to their chemical composition and carrier concentrations. Like in semiconductor materials, the carrier concentration of the superconductor cuprates can be varied by doping process. Doping process typically refers to introduction of impurities or charge carriers that can be holes or electrons. It is known that Mott insulators are parent compound of cuprate superconductors and the superconductivity become dominant when they are doped away from stoichiometry. It can be seen from the Figure 2.12, the temperature-charge carrier concentration phase diagram of these cuprates is parabolic. Two regions of the phase diagram which are antiferromagnetic insulating state (AF)-below 320 K with hole doping value of $p \leq 0.02$ and the superconducting state (SC)-below 100 K and doping value changes between 0.06 and 0.26 can be seen obviously in the Figure 2.12 . The superconducting region in the phase diagram can be classified into three different regions; underdoped region where T_c seems to be decrease while the level of doping decreasing, optimally doped region where T_c reach its maximum value and finally overdoped region where T_c decreases while doping level goes further. For this reason, some superconductor properties such as critical current density and transition temperature can be altered by changing the doping level. Furthermore, the structural and flux pinning properties of the high temperature superconductors cuprates can be altered by doping level to obtain suitable superconducting material for applications at higher temperatures and fields. Moreover, doping is very important to understand the mechanism of high temperature superconductors. For instance, when an impurity atom is substituted into a system, the atom strongly perturbs the surrounding electronic environment and so, can be used to probe HTS at atomic scale.

In high temperature superconductors, charge carries can be in the form of holes which are inserted by oxygen doping as in $Bi_2Sr_2CaCu_2O_{8+x}$, by substituting a monovalent atom with a divalent atom like in $La_{2-x}Sr_xCuO_2$, or by removing oxygen atoms as in $YBa_2Cu_3O_{7-x}$. Hole doping is the most common method for changing the oxygen content since it causes some differences in the occupation of sites in the chain layers which also known as charge reservoirs layers, while oxygen sites in the ab planes are always fully occupied. The oxygen atoms are always available between any two nearest Sr or Bi atoms. And the Cu-O planes are regarded to conduct suppercurrent. Therefore, the transition temperatures of such superconductor are strongly related to the number of Cu-O layers in a unit cell of the superconductor. In a unit cell, the Cu-O layers are separated by other atoms. The layers can be divided into two categories which are structural layers and charge reservoirs. The structural layers play a minor role in the value of T_c, however, the charge reservoirs have an important effect on T_c. The distance between Cu-O planes and the charge reservoirs layer, which provides charge reservoir into the Cu-O planes, are also very important.

The other important property is that electrical conductivity, which can be improved by doping of Cu-O planes. Doping provides the electrons removing from the planes and leaving behind holes. Finally, when the holes are sufficient, the Cu-O planes act as a metallic to become superconducting. Therefore, the transition temperature strongly related to the carrier concentrations in the Cu-O planes.

Furthermore, Hall effect measurements revealed that the charge carriers in the HTS superconductors are generally holes. However, there also exist electron-doped cuprates such as $Pr_{2-x}Ce_xCuO_{4-d}$, where Pr can replaced by Nd or Sm.

In addition, it is known that crystal structures of high temperature superconductors are anisotropic. Therefore, due to the this anisotropy, Cu-O planes show high electrical conductivity while the conduction perpendicular to the Cu-O planes is less by amount two to four orders of magnitude which related to the specific compound and the quality of the crystal used. The Figure 2.13 shows the temperature dependence of c-axis resistivity of Bi2212 samples having different doping levels. It can be seen obviously that the c-axis resistivity of the samples are increasing when the doping level is decreasing (Watanabe, et al.1997).

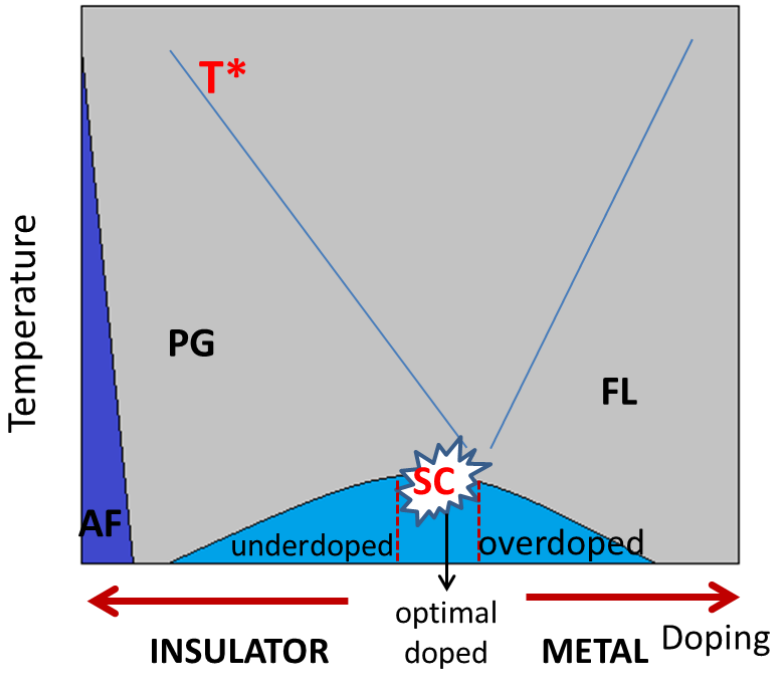

Figure 2.12. The phase diagram with doping in high-T_c cuprates superconductors

The doping of high temperature cuprates have an important effect on some other superconducting properties such as energy gap and superconducting energy gap of underdoped Bi2212 crystal is found to be larger than the optimally doped and overdoped samples. Furthermore, it is known from the previous studies that the energy gap value is decreasing when the hole doping is increasing (Miyakawa, et al. 1998).

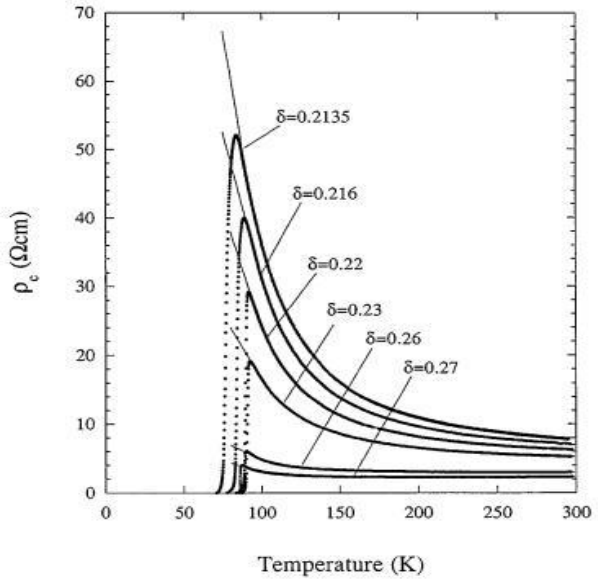

Figure 2.13. c-axis resistivity of $Bi_2Sr_2CaCu_2O_{8+d}$ versus temperature for different doping levels (Source: Watanabe, et al. 1997)

2.10. Objective of the Work

Rapid increase in applications of the electromagnetic waves in the terahertz frequency range requires new techniques to obtain continues-wave terahertz radiation sources. Hence, small, continuous, high power solid-state terahertz sources are needed for piratical applications. High temperature superconductor $Bi_2Sr_2CaCu_2O_{8+\delta}$ (Bi2212), which are constructed from a stack of several intrinsic Josephson junctions (IJJs), is a good candidate to obtain desired terahertz radiation. Also, Bi2212 layers are unique structures, in which the superconducting (CuO_2) and insulating (Bi-O) layers are alternately stacked within a unit cell. Therefore, mesa shaped structure from Bi2212 single crystal can be used to obtained intense coherent continuous emission in the frequency of terahertz regime.

THz emitting mesas are below a certain under-doped level, which has relatively small critical current unlike optimally doped and over-doped Bi2212 samples. However, while the mesa dimension is increasing, the back bending of the current-voltage curve is seen due to the large volume of the mesa causes self-heating. In this study, our aim is to find the critical current density dependence of mesa area to obtain maximum emission power for the terahertz radiation.

In this work, we have fabricated rectangular triple mesa structures from Bi2212 single crystal using e-beam lithography and ion beam etching techniques. After mesa fabrication process, SEM, surface profilometer and atomic force microscope were used to find exact dimensions of the fabricated triple mesa structures as 300×50, 200×50 and 100×50 μm^2, respectively. In order to characterize the Bi2212 mesas, c-axis resistance versus temperature (R-T), and current-voltage behavior (I-V) were measured in a He flow cryostat. We have studied variation of Josephson critical current density of mesas with different dimensions.

CHAPTER 3

EXPERIMENTAL

3.1 Annealing of Bi2212 Single Crystal

After the discovery of Bi-based superconductors by Maeda et al in 1988, many scientists have made extensive efforts to understand the structure of high temperature superconductor materials (Maeda, et al. 1988). It is well recognized that Cu-O planes in the high temperature superconductors have an important role in determining of carrier concentration, which provides important knowledge about physical properties of high temperature superconductors. To control the carrier concentration of cuprates, the oxygen site occupancy should be altered by annealing process with controlled oxygen partial pressure. Here, oxygen non-stoichiometry is very crucial parameter to control critical temperature of Bi2212 single crystal. It is shown that the critical temperature of Bi22212 crystal can be changed significantly by controlled heat treatment in different atmospheres (Genoud, et al. 1995). When the oxygen concentration is lower (higher) than the optimal one, the crystal said to be underpoded (overdoped). Three different atmospheres such as argon, vacuum, or oxygen can be used to control oxygen level of Bi2212 crystal. Also it is recognized that annealing of Bi2212 systems in air alters the superconducting transition width, critical temperature, c-axis resistivity and critical current of IIJ and also annealing time has an important effects on mechanical properties such as the micro hardness, elastic modules and bulk density (Khalil, et.al 2000).

In the previous studies, it has been shown that the THz emitting mesas are below a certain under-doped level which has relatively small critical current unlike optimally doped and over-doped Bi2212 samples (Ozyuzer, et al. 2009). Therefore, we fabricated a set of samples with various doping levels and sizes and the heat treatment duration is varied to change the T_c and critical current of crystals.

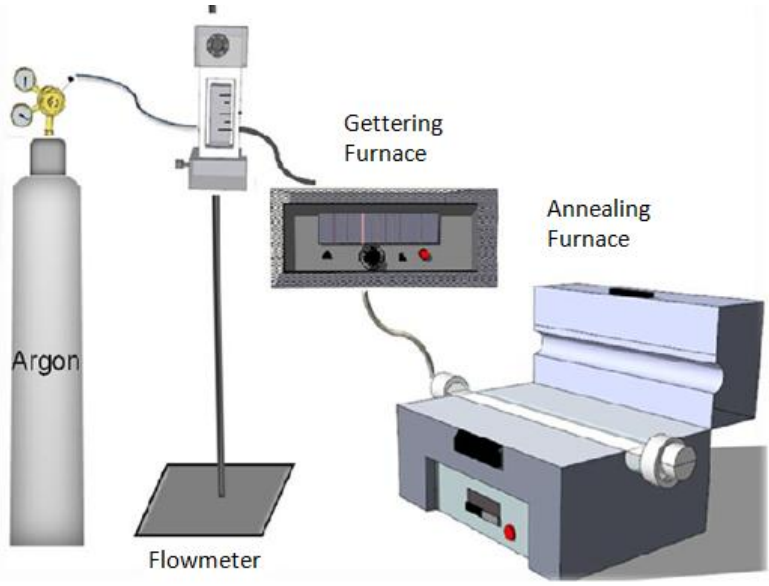

Figure 3.1. Our annealing system in Argon atmosphere
(Source: Demirhan 2011)

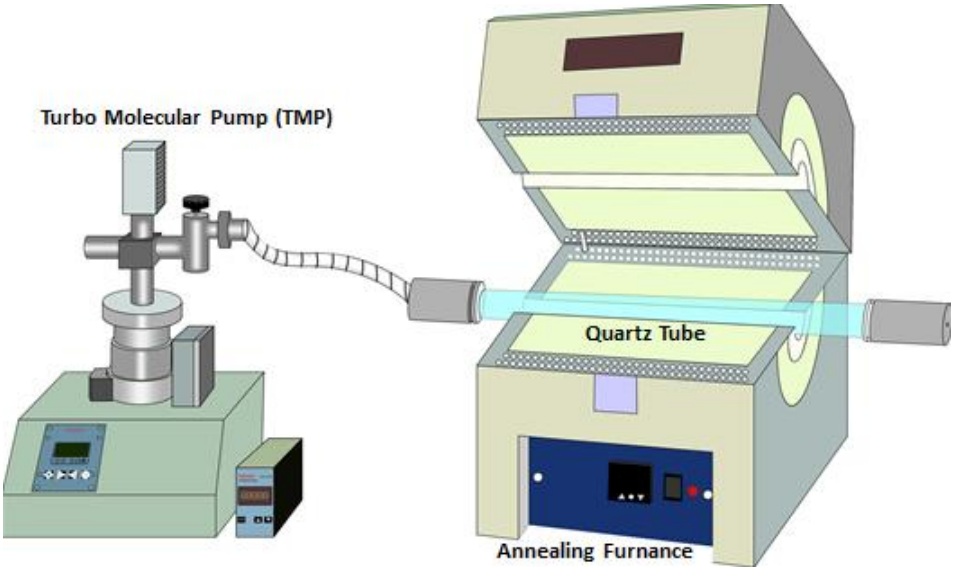

Figure 3.2. Annealing system under vacuum

In the first annealing set up, we have used Ar gas to anneal our samples. As seen in the first experimental set up, we have used a gas flowmeter, gettering furnance and a annealing furnance for this process. We have placed our samples in a crucible and then placed in to the quartz tube as seen in the Figure 3.1. After that 100 sccm Argon gas is used during the annealing process right after purification. However, we have determined

that this way to anneal the as-grown Bi2212 samples is not good enough. Therefore, to anneal as grown Bi2212 single crystals, we have used a turbo molecular pump and a furnace with a quartz tube. Firstly, turbo molecular pump is used to reach desired pressure value before starting the annealing procedure. After that, we have operated the furnace to desired temperature and time as seen in the Figure 3.2.

3.2 Mesa Fabrication Process

This chapter contains experimental setups, which are used in fabrication of triple mesa structure for this thesis. The fabrication procedure of micron sized mesas on Bi2212 crystals are presented in the first part. Then, characterization methods of the samples including resistance versus temperature R-T, current versus voltage I-V characteristics and Golay cell measurement are explained in details.

3.2.1. Thermal Evaporation

In this work, we have used annealed Bi2212 single crystals, which were grown using floating zone method by Prof. Kadowaki at University of Tsukuba in Japan and Prof. Miyakawa at Tokyo University in Japan. For fabrication of triple mesa structures on the surface of annealed Bi2212 single crystals, firstly, single crystal of Bi2212 is glued onto a sapphire substrate from its smooth a-b surface by silver epoxy as seen in Figure 3.3 a. Here, we have used the silver epoxy and sapphire substrate since they are perfect thermal conductors. Furthermore, the differences between crystal temperature and measured temperature on cold head by sensor affect the electrical results on mesa. Then the crystal was cleaved using an adhesive tape as seen in Figure 3.2.b. After that, the sample is immediately placed in vacuum chamber to evaporate 100 nm gold layer onto it. Because the evaporated gold layer protects the fresh and smooth layer of Bi2212 from chemicals such as photoresist, developer and water during the lithography. In addition, it is very useful to get electrical contacts for characterization.

Schematic representation of the vacuum thermal evaporation system that we have used to deposition of Au layer on cleaved Bi-2212 single crystals can be seen in the Figure 3.4. Evaporation technique based on two basic processes, which are evaporation of material in a filament boat and then condensation on the cooler substrate.

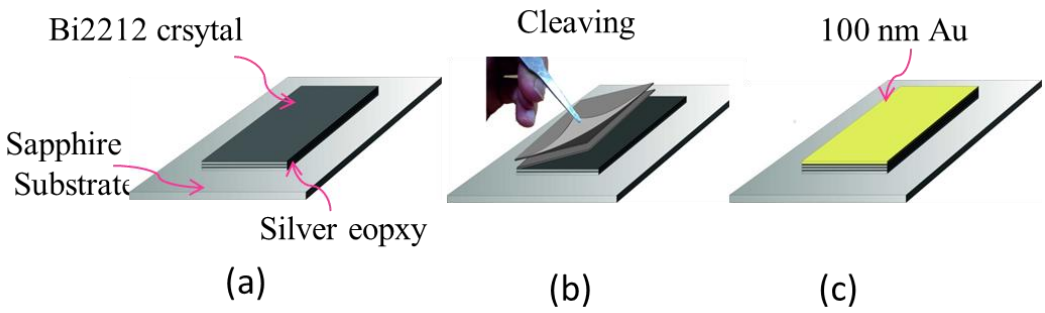

Figure 3.3. The steps in the beginning for the mesa fabrication a) Adhesion of crystal on substrate b) Cleaving crystal c) Gold layer deposition

To evaporate the material, the boat should be heated by high current source since evaporation of materials requires high temperatures. In addition, the current that should be used depends on filament boat's shape, i.e. resistance. In our system, the value of current passing through the filament boat has been kept constant between 65 and 70 A. The material in the boat condenses in the form of thin film on the surface of the substrate and on the walls of the evaporation chamber. During the evaporation, generally low pressures about 10^{-6} Torr are preferred to avoid reaction between the vapor and atmosphere. Because at these low pressures, the mean free path of vapor atoms and the vacuum chamber dimensions are approximately same, so, it results in traveling of particles in straight lines from the source to substrate. During the evaporation, the deposited film thickness and the rate of deposition are controlled by a thickness monitor using a quartz crystal. Here, the quartz crystal should be cleaned periodically to obtain precise results. Also deposited film thickness is controlled by a shutter that also prevents thin film from contaminations coming from the boat at the beginning of the evaporation.

Vacuum thermal evaporation technique has some advantages; the average energy of vapor atoms, which are reaching the cooler substrate, are generally very low, in the order of kT, i.e. tenths of eV. The process utilizes high vacuum environment, and so provides very high purity of thin films. Furthermore, the deposition rate is high and the technique has fewer tendencies for unintentional substrate heating.

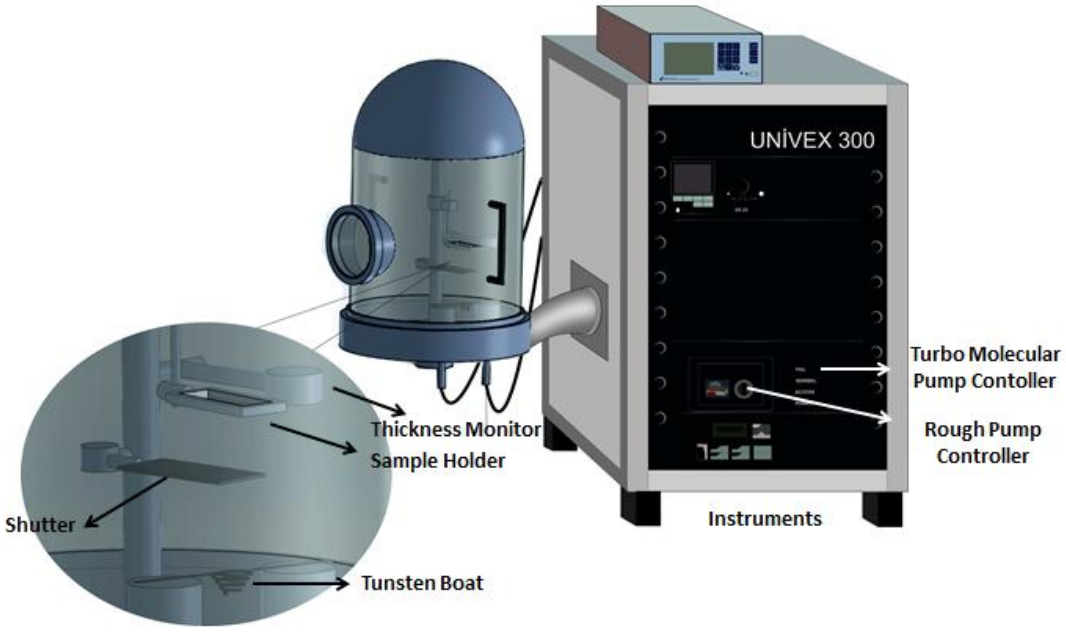

Figure 3.4. Schematic of our thermal evaporation system

3.2.2. E-beam Lithography Process

Electron beam lithography is a useful technique to produce extremely fine patterns (~50 nm) and provides scientist to design and place elements at the smallest possible scale. This technique derived from the early scanning electron microscope, consists of scanning a beam of electrons across a surface covered with a resist film, which is sensitive to those electrons. The main attributes of the technology are; it provides very high resolution for patterning process, i.e. at the nanometer scale. This process does not require a photo mask unlike classical photolithography process. However, with such precision, e-beam lithography technique has some limitations. Firstly, patterns can only be obtain in a long period of time and it is a disadvantage for commercial acceptance. Besides, since electrons are charged particles, e-beam lithography requires high vacuum conditions so it further complicates the required equipment and processes. Despite of the fact that electron beam lithography's parts required are very complicated, the process of e-beam lithography is quite simple. Therefore, it is more beneficial to concentrate some of the important components of electron beam lithography to work efficiently.

Electron Gun; Electron gun, an aperture that is capable of shooting a beam of electrons in a specific direction, plays an significant role in e-beam lithography process.

There is an emitter that first heated to create electrons and then a high voltage is applied to make electrons accelerated through the surface, which is also called as anode. When the applied voltage is altered, the trajectory and the focus of electrons can be shifted.

Electron Optical Column; Electron beam column is capable of correcting the beam of electrons through a desired direction. There are two parallel plates that can be charged electrostatically to result in an electric field to bend the beam in a desired direction.

Surface; After that the optical column is used to direct and concentrate the beam; electrons are ready to be focused towards the surface. Like other lithography techniques, photoresist is used to cover the whole surface. Technically, energetic bombardment of electrons led to breakage of bonds in any type of polymer. When the electron beam is reached to the surface, either additive or subtractive reaction occurs. The former uses the electrons to induce a deposition on the surface while the latter is to remove the sections of the resist and surface.

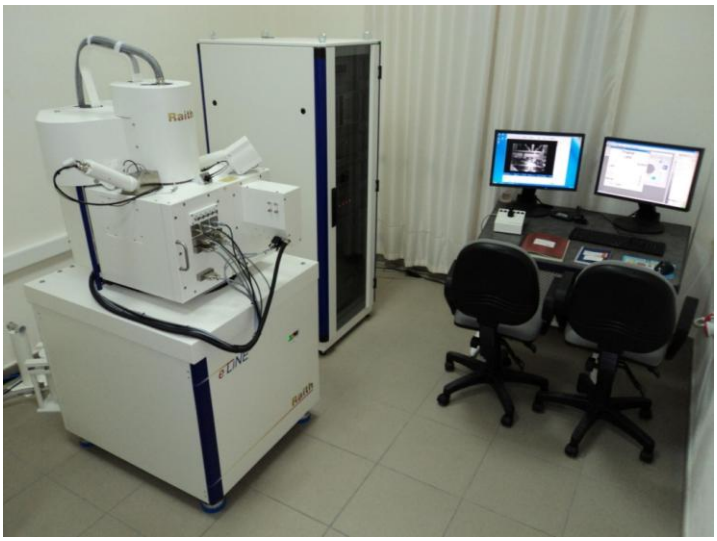

Figure 3.5. Picture of our electron beam lithography system

In our study, we have followed several processes to create triple mesa structures from Bi-2212 single crystal. First, we have used AZ5214 type photoresist, which is spun onto our sample at 3000 rpm for 60 seconds. Then the sample is soft baked using an oven at 90 ^{o}C for 30 minutes to make it ready for e-beam lithography process. For patterning process with e-beam lithography technique, we have used 5 kV e-beams to

create desired triple mesa structure with areas of 300 × 100, 200 × 50 and 100 × 50 μm^2 on the same Bi-2212 crystal.

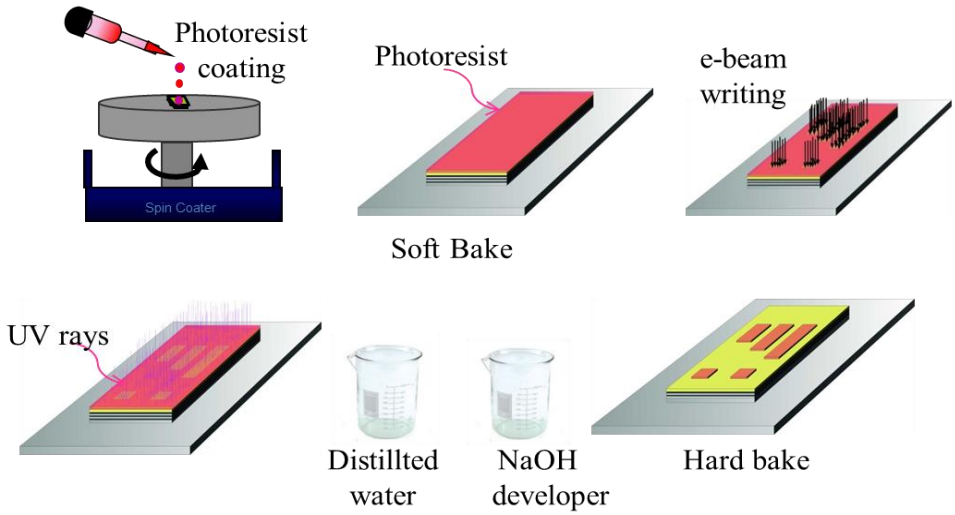

Figure 3.6. Schematic representation of e-beam lithography process

Figure 3.5 represents the e-beam lithography system that we used to fabricate the mesa structures. Afterwards, sample is exposed to UV lights for 7 seconds and then immediately developed in 2 M NaOH solution for 25 seconds. Before starting etching process, firstly sample is hard baked in an oven at 120 ^{o}C for 30 minutes. The schematic diagram of the steps can be seen in the Figure 3.6. Now, sample is ready for etching.

3.3.3. Ion Beam Etching

Among many etching techniques, chemical and dry etching processes are the most commonly used methods in micron-sized fabrication of materials. Chemical etching processes have some disadvantages such as limiting lifetime due to contamination, undercutting of films, chemical reactions with other materials and surface roughness and pitting. Because of this reason, this technique is not suitable for patterning of mesa structures. In contrast to that, ion beam etching is a stress free physical process whereby an ion source is used to produce broad ion beam, which are directed to the substrate for etching purposes. Argon atoms are ionized in a chamber by electron bombardment. Here electrons are generated by a cathode filament and then collected by the anode and here generally a magnetic field is used to direct the electrons

to the right place and to increase the probability of etching. A turbo molecular pump with a rough pump is used to reach the pressure value of 10^{-6} Torrs. Low pressure is necessary to produce the ion beam plasma and to decrease the contamination of substrate during etching process.

In our study, after photoresist is shaped on the 100 nm gold layer of Bi-2212 single crystal by e-beam lithography technique, the next step is placed the sample in argon ion beam etching system to etch down unprotected area. In our experimental setup, samples are placed inside the etching chamber with an angle of 67.5^{o}. The Figure 3.7 illustrates the schematic of our ion beam system in our laboratory. Before starting the etching process, firstly etching chamber is pumped using a turbo molecular pump with back pump until the pressure value of 10^{-6} Torrs. Because low-pressure values are required to increase the mean free path of ion beam accelerating from the ion source. When desired pressure values are reached, firstly argon gas, which is controlling mass flow controller, is introduced to the system. In our etching experiments, we have used 30-sccm Ar gas. Afterwards, a dc source is applied to obtain plasma inside the etching chamber and a rotational feed through mechanism is used to prevent the differences in lateral angles of mesas. During etching process, accelerated argon ions and crystal atoms collide each other and produce heating. Therefore, we have used a cooling system to cool the sample holder to prevent the heating occurrence throughout the etching experiments.

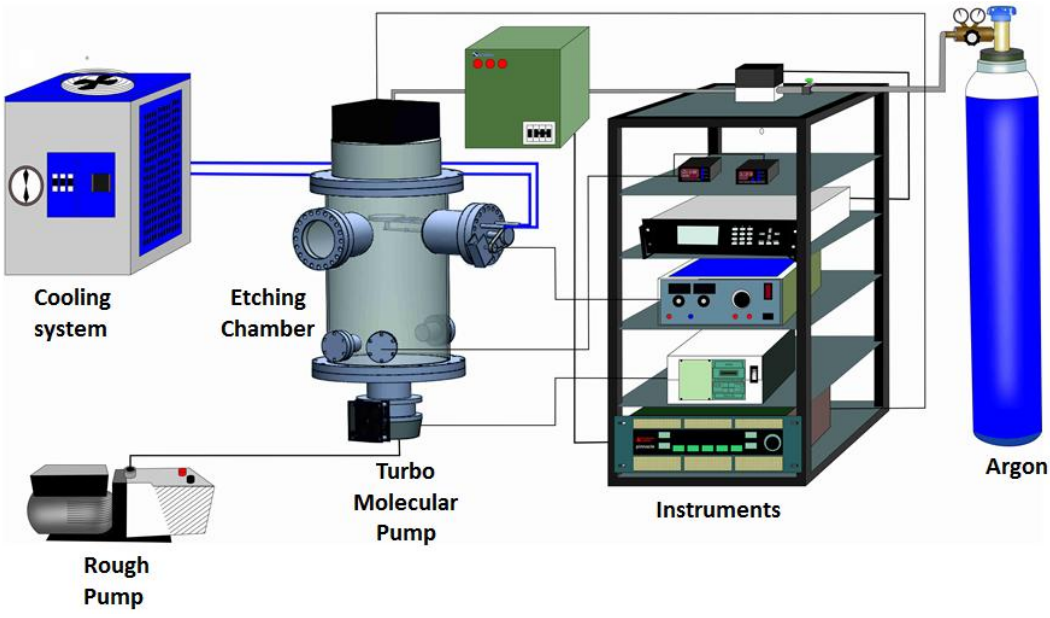

Figure 3.7. Schematic picture of our ion beam etching system

Since the protected area is not etched, when the sample is placed in acetone to clean up remained photoresist, we finally obtain triple mesa structures with height of approximately 700-1200 μm as seen in Figure 3.8.

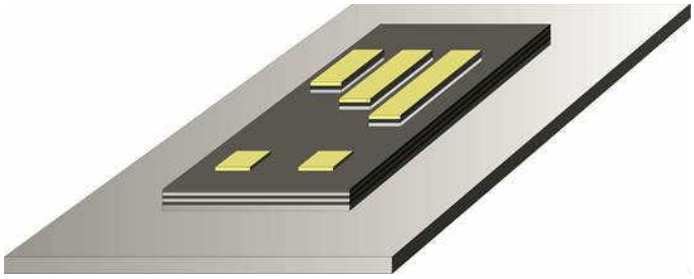

Figure 3.8. Schematic of triple mesa structure

3.3.4. Gold Stripe Fabrication

Since fabricated mesas have very small areas of 300 × 100, 200 × 50 and 100 × 50 μm^2, making a contact on them is very difficult to do. For this reason, we have deposited 200 nm CaF_2 insulating layer by vacuum thermal evaporation technique as seen in Figure 3.9 (a).

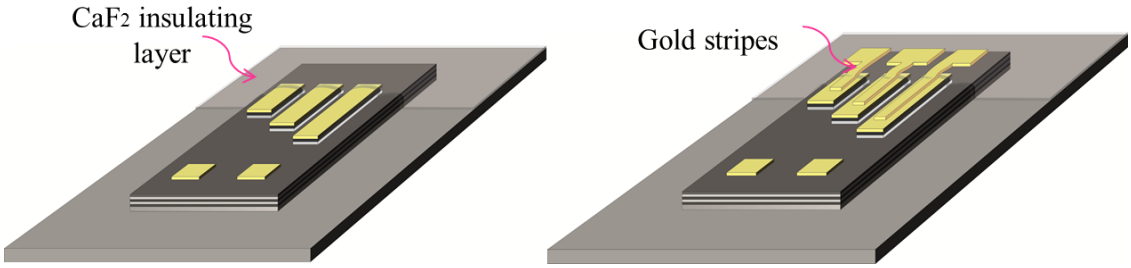

Figure 3.9. a) CaF_2 deposition onto crystal and small part of mesa b) Gold stripe deposition on mesa and CaF_2 layer

After depositing the insulating layer, the next step is fabrication of gold stripes using e-beam lithography technique. Firstly, PMMA 200 K spun onto the sample for 45 seconds at 3000 rpm and then sample is soft baked using a hot plate at 170 ^oC for 90 seconds. Then, PMMA 950 K is coated by spin coater for 45 seconds at 4000 rpm. Then, sample is again soft baked using a hot plate at 170 ^oC for 90 seconds. After that, e-beam lithography technique is used for patterning of 200 μm length and 30 μm width

gold stripe. At this time, 20 kV e-beam is used for exposure. When the exposure is completed, sample is developed in 1:2 MIBK:IPA (Methyl Isobutyl) for 90 seconds.

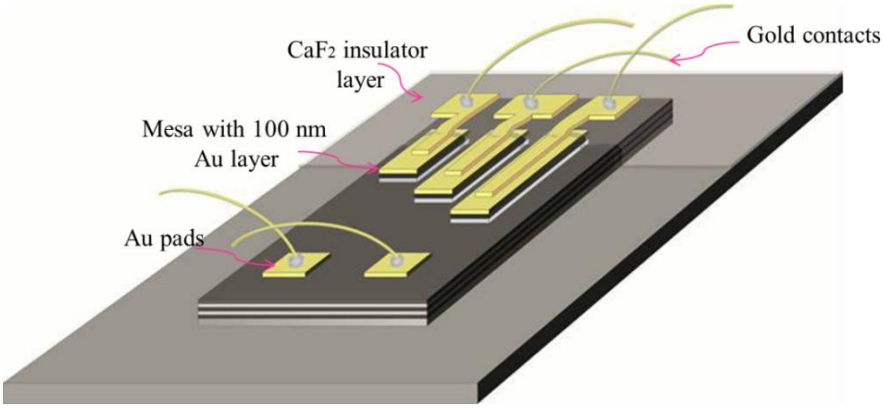

Figure 3.10. The final measurement configuration of mesa structure

After that 200 nm Au layer is deposited on sample to create a gold stripe for making a contact on small area of mesa. Finally, sample is placed in an acetone and distillate water solution to obtain final configuration of triple mesa structure. The Figure 3.9 (b) illustrates the gold stripe deposition on mesa and CaF_2 layer. Eventually, silver epoxy, which is a good conductor, is used to connect three gold wires to the triple mesa structures to characterize them as seen in Figure 3.10.

3.3.5. R-T, I-V and Golay cell Measurements

For characterization of fabricated triple mesa structures to observe the Josephson critical current density and other important superconducting properties, c-axis resistance versus temperature (R-T), and current-voltage behavior (I-V) were measured in a He flow cryostat system. In this measurement system, a closed cycle cooler is used to decrease the temperature of fabricated triple mesa structure from room temperature to 20 K. Here, He gas is compressed to 16.5 bar using a water cooled compressor to expand it in the cold head for cooling the sample. The compressed He gas is transferred by a flexible line to the cryostat. Cooling due to the expansion of He gas is controlled by a temperature controller. In this system, we have used low-pressure values before beginning the measurement since it is required to create a thermal isolation and prevent the cooling system form ambient thermal effects. In order to sustain thermal isolation

between the sample holder and shield of the cryostat, a mechanical pump is used to decrease the pressure of the region. The vacuum value should be 10^{-4} or 10^{-5} mbar to reach required low temperatures. The closed cycle cooling system has many advantages such as that it is very economical system, which includes closed cycle cooling without loss of He gas. In addition, it contains a temperature controller that is connected to the heater and compressor provides us controlling the system temperature.

By using the system mentioned above, we have done resistance versus temperature and current versus voltage measurements to characterize the fabricated triple mesa structures. Schematic representation of the measurement system can be seen in Figure 3.11. In this system, the experimental setups are controlled by a program written in Lab-view. The Lab-view program is also used to analyze and storage of obtained data. Furthermore, this program enables us to see the drift of the experimental result during the measurement and its block program is very suitable to make some differences to create a new experimental measurement steps.

When the temperature is decreased using a closed cycle cooling system, at the same time, the variations on the mesa resistance is measured. The R-T measurement system consists of a voltmeter, current source and temperature controller. The applied current value is kept constant during the R-T measurement. To obtain more precise results, current is applied from both positive and negative side rapidly using a current source. After that the average value of the resistance is used by Lab-view program.

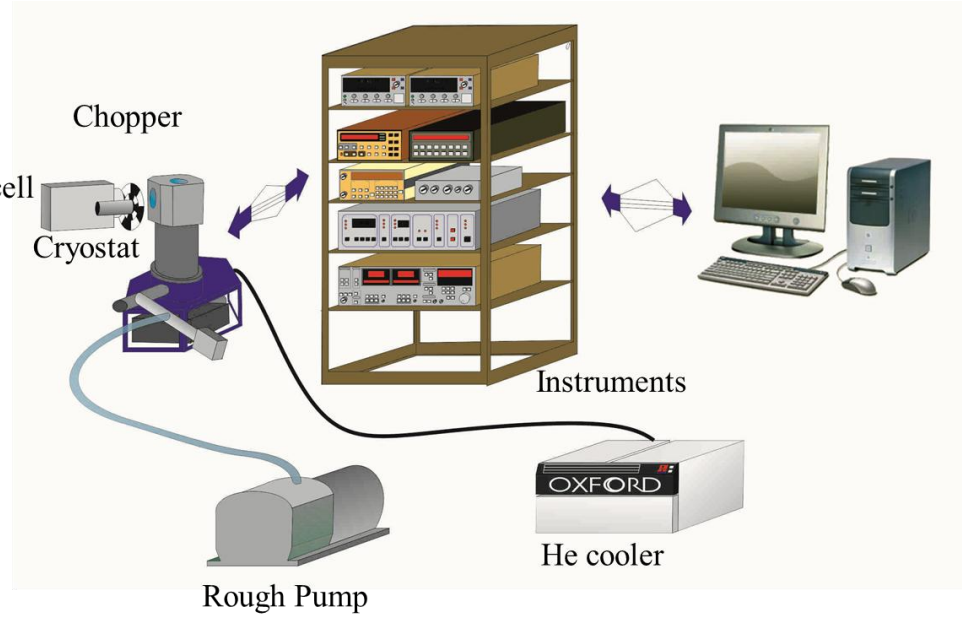

Figure 3.11. The schematic of our He flow cryostat system

The experimental set up consists of two voltmeter, a function generator and a oscilloscope as seen in the Figure 3.11. The reason of using two voltmeters is to measure the voltage of mesa and the applied current on resistance. Here the resistance is serially located between function generator and mesa.

In order to apply current with desired frequencies and amplitudes during I-V and Golay cell measurements, a function generator is used in this set up. In addition, a heater is used to keep constant the sample's temperature during the I-V measurement. When the applied current's amplitude is increasing to the higher voltage values, current with low frequency (0.0003 Hz) is used to obtain the I-V cure with hysterical behavior and much quasi-particle branches. The reason of using an oscillator is to observe the voltage jump and I-V drift before starting to measurement.

Golay cell measurement and I-V measurement were done to detect the emission power of fabricated mesas at the same time. When the applied current is swept slowly by a function generator, the Golay cell measurement was obtained from the long side of the mesa structure. In this set up, also a chopper with chopping frequency of 70 Hz is used to modulate emission of radiation to pulse. Output signal from Golay cell is amplified by lock-in amplifier and it refers to emission power of radiation emitted from mesa.

CHAPTER 4

RESULTS AND DISCUSSION

4.1. Structural Characterization

In this section of the thesis, I will mention about structural characterization of the fabricated mesas. Briefly, after the mesa fabrication, surface profilometer and atomic force microscope were used to obtain the exact dimensions of each mesa. In order to characterize the Bi2212 mesas, c-axis resistance versus temperature (R-T), and current–voltage (I-V) behavior were measured in a He flow cryostat. The details of the characterization will be given in the following sections.

4.1.1. Optic Microscope Images

To examine the fabricated triple mesa structures using optical microscopy is very beneficial in terms of having an idea about the surface of the mesas. In addition, this characterization provides us some useful information about the quality of the e-beam lithography process. In other words, some problems come from the lithograph and etching process such as contamination onto the surface of the crystal, remaining of photoresist skin after etching or excess or insufficient etching. Therefore, this pre-characterization of the each step of mesa fabrication is very useful to understand mesas conditions at the beginning of the investigation.

Before starting the e-beam lithography process, annealed Bi2212 crystals are cleaved using a scotch tape to obtain a fresh and smooth surface of the crystal. It can be obviously seen from the Figure 4.1 that, the cleaved crystals have very smooth and clean surface. Figure 4.2 represents the optical microscopy images of the mesa structures with various areas. The areas of the mesas are 50×300, 50×200, 50×100 μm^2, respectively. After fabricated these mesa structure, the gold stripes are composed by electron beam lithography technique as shown in the Figure 4.3.

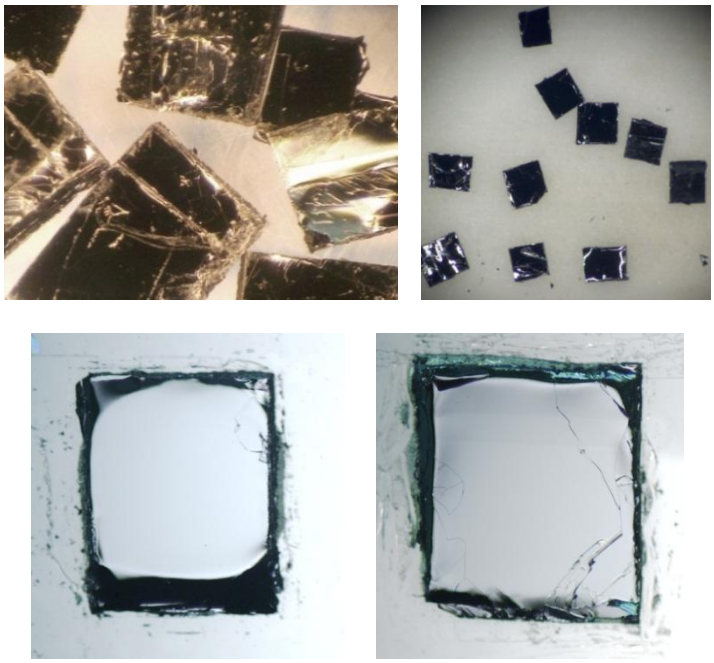

Figure 4.1 Optical images of crystals before and after annealing

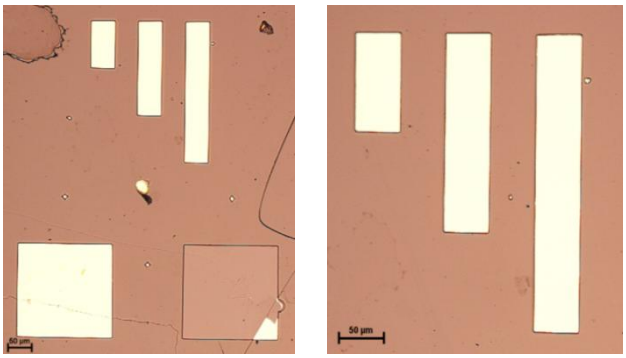

Figure 4.2. Optical images of HS14 after mesa fabrication

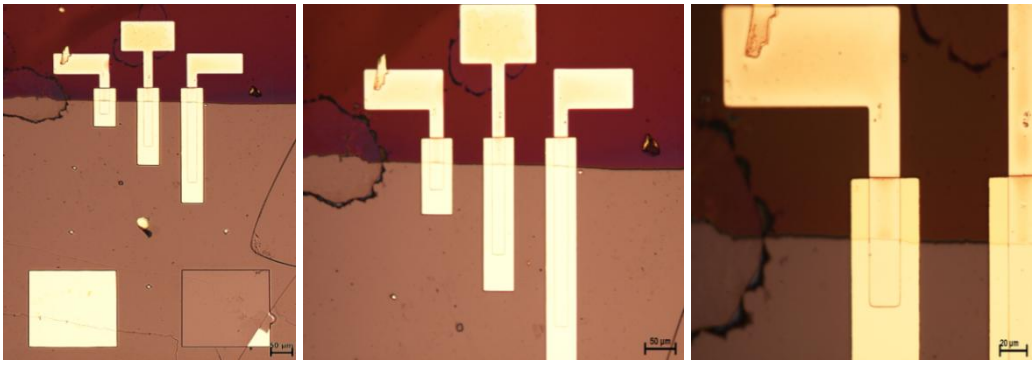

Figure 4.3. Optical image of HS14 after gold stripe fabrication by lift off technique

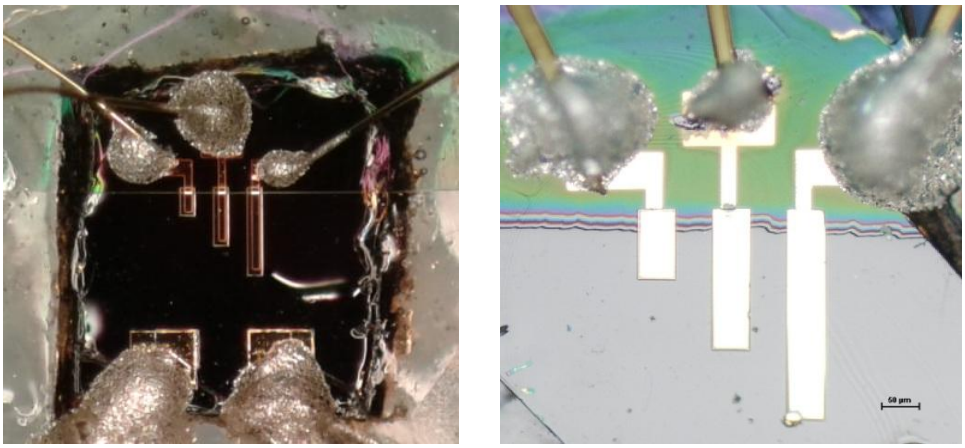

Figure 4.4. Optical images of HS02

Finally, in order to characterize the triple mesa structures, we have placed three gold wires onto the mesa structures with gold stripes. In the Figure 4.4, CaF_2 insulating layer on mesas also can be seen.

4.1.2. SEM and Profilometer Results

From the previous studies, it is demonstrated that the side of the mesa is very important parameter since it leads to impedance mismatch between Bi2212 and vacuum (Ozyuzer, et al. 2007).

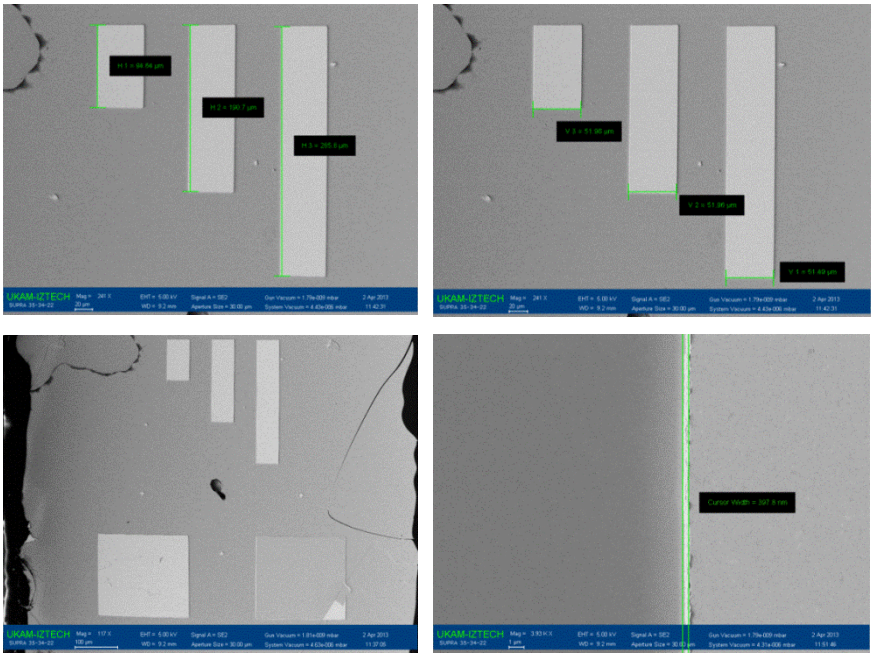

Figure 4.5. SEM images of HS14

Also Koshelev et al. revealed that the lateral angle of fabricated mesa should be nearly right for terahertz emission (Koshelev 2008).

Because of this reason, SEM and surface profilometer are used to determine the exact dimensions of the mesas. We have used SEM to image roughness of the side faces of the mesas and profilometer is used to determine exact height (c-axis) including 100 nm gold layer. Therefore, we have subtracted the 100 nm deposited Au layer from the height of total thickness of the mesa. It is know that, one SIS junction size in a unit cell is about 1.5 μm, so, we have divided the total mesa height by the size of a SIS junction to calculate the number of junctions. For instance, 1 μm height of mesa contains approximately 670 IJJs.

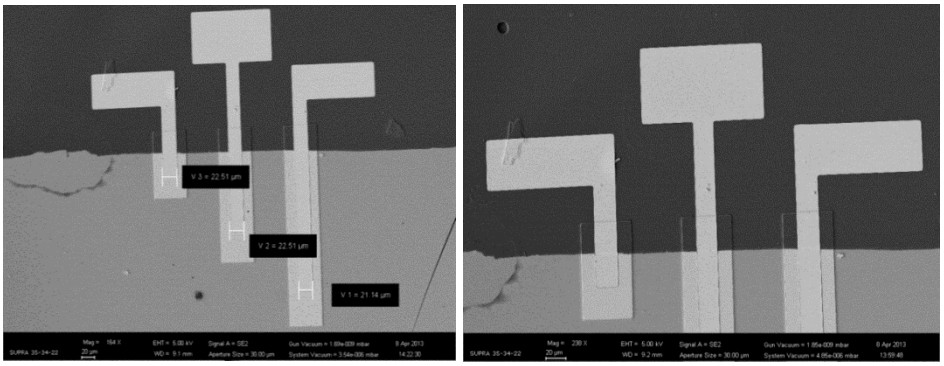

Figure 4.6. SEM images of HS14

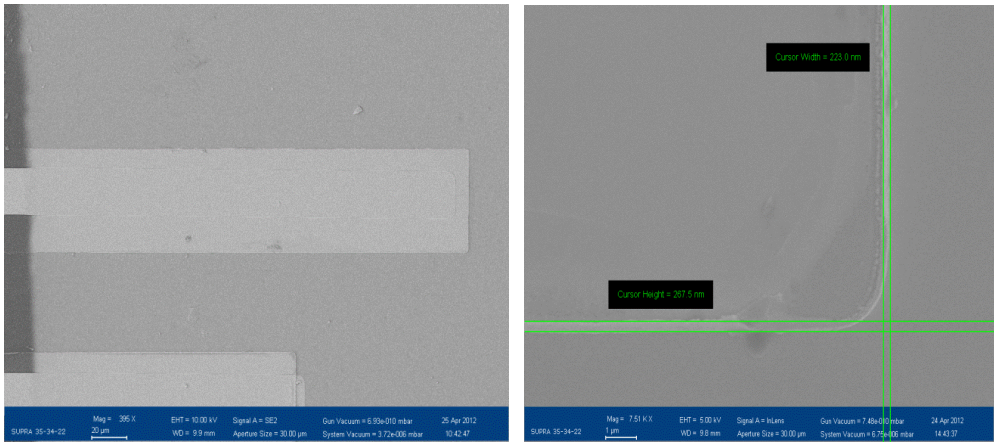

Figure 4.7. SEM images of HS02

Figure 4.5. and Figure 4.7. illustrate that the fabricated triple mesas are trapezoidal, which means that they have narrow top and wide bottom. The reason of obtaining these trapezoidal shapes is thick photoresist layer since photoresist shades the

region at the edge of the mesa to protect them from etching process. Therefore, when the mesa height is increasing, mesa starts to spread out.

Figure 4.8. Step-height analyses of HS02

Here, the differences between the basal plane and the side of the mesa can be found using SEM pictures. In addition, when we look at the Figure 4.8, we can see that the height of the mesa is about 900 nm, which includes 100 nm gold layer. Therefore, when we subtract the thickness of the gold layer, we can state that the mesa has approximately the thickness of 800 nm. Hence, using the length difference between basal plane and side of the mesa and the measured thickness of the sample by profilometer gives us the lateral angle just by using the simple Equation (4.1). For HS02 sample, the calculated lateral angle is almost 70^{o}.

$$\theta(lateral \quad angle \quad of \quad mesa) = \tan^{-1}\left(\frac{profilometer \quad data \quad (c-axis)}{SEM \quad data \quad (a-axis)}\right) \tag{4.1}$$

We have calculated all the lateral angles of the fabricated mesas as seen in the Table 4.1, Table 4.2 and Table 4.3, which belong to HS01, HS02 and HS11 sample, respectively. The tables also includes some other information such Au height, mesa dimension and doping time of the mesas.

Table 4.1. Height of mesas and deposited thin films for HS01

Mesa type	Mesa height	Au height	Mesa dimension	Doping time
HS01a	~832 nm	~100	50 x 300 μm^2	As-grown
HS01b	~830 nm	~100	50 x 200 μm^2	As-grown
HS01c	~852 nm	~100	50 x 100 μm^2	As-grown

Table 4.1. represents the results of HS01 sample, which is fabricated on as grown Bi-2212 single crystal. The mesas have height of 832, 830 and 852 nm for mesas with areas of 50 × 300, 50 × 200 and 50 × 100 μm^2, respectively. Ozyuzer et al showed that the mesa should contain more than 500 IJJs to obtain high power terahertz radiation (Ozyuzer, et al. 2007). Therefore, when we look at the Table 4.1, all fabricated mesas are suitable for terahertz radiation.

Table 4.2. Height of mesas and deposited thin films for HS02

Mesa type	Mesa height	Au height	Mesa dimension	Doping time
HS02a	~820 nm	~100 nm	50 x 300 μm^2	7 hours 425 ^{0}C
HS02b	~840nm	~100 nm	50 x 200 μm^2	7 hours 425 ^{0}C
HS02c	~830 nm	~100 nm	50 x 100 μm^2	7 hours 425 ^{0}C

Table 4.2. illustrates the height of the mesas and other information about HS02 sample. The crystal used for this sample is annealed at 425 ^{o}C for seven hours. In addition, the thickness of the mesas which are on the same annealed crystal, changing between 820 nm and 840 nm.

Table 4.3. provides information about HS11 sample, which is annealed at 450 ^{o}C for four hours. Also the thickness of the mesas changing from 760 nm to 780 nm. In conclusion, it can be stated that the dimensions of the mesas are suitable to obtain high power and high frequency terahertz radiation.

Table 4.3. Height of mesas and deposited thin films for HS11

Mesa type	Mesa height	Au height	Mesa dimension	Doping time
HS11a	~780 nm	~100 nm	50 x 300 μm^2	4 hours 450 ^{0}C
HS11b	~766 nm	~100 nm	50 x 200 μm^2	4 hours 450 ^{0}C
HS11c	~760 nm	~100 nm	50 x 100 μm^2	4 hours 450 ^{0}C

4.2. Electrical Measurement Results

After the triple mesa structures were fabricated, three-probe contacts were taken to measure c-axis resistance versus temperature (R-T), and current–voltage (I-V) behavior in a (He) Helium flow cryostat. In this section, the details of the R-T and I-V measurements will be mentioned.

4.2.1. Temperature Dependence of c-axis Resistance in Bi2212

Temperature dependence of c-axis resistance of the mesas from Bi-2212 crystal is observed using a closed cycle Helium cooling and continuous flow He cryostat systems. First of all, when we look at the all R-T graphs, it is seen that all fabricated mesas show sharp transition from normal state to superconductor state. Some properties about these transitions can be seen in the Table 4.4, Table 4.5 and Table 4.6. As seen in these tables, the transition temperature values are different. One of the reasons for this situation is differences in oxygen doping levels. Furthermore, all mesas show characteristic behaviors of temperature dependent resistance of Bi-2212 single crystal. Figures represents that all mesas show exponentially increasing resistance from room temperature to transition temperature. When the temperature is reached to the transition temperature, a sharp drop is observed for all mesas. Moreover, the ratios of R_{Tc}/ R_{300K} are changing between 1.14 and 2.90 for all fabricated mesas. When the temperature is below the critical temperature of the Bi-2212 crystal, there is an increase in resistance of the sample due to the contact resistance coming from three-point measurement

configuration and the interface between the gold layer and the top surface of the Bi2212.

The Table 4.4 provides information about the electrical properties of HS01 sample, which was fabricated onto as grown Bi2212 single crsytal. For this sample, the contact resistance values are very high as seen in the Table 4.4. This may be as a result of the interface between the gold layer and the Bi212 crystal. However, the ΔT_c values for this sample are changing between 0.4 and 1.3. This means that the crystal doesn't have too much defect.

Table 4.4. Electrical properties of HS01

	$R_{Tc(onset)}$ (ohm)	$R_{300\ K}$ (ohm)	$R_{contact}$ (ohm)	$R_{(Tc)}/R_{300K}$	$T_{c(onset)}$ (K)	ΔT_c (K)
HS01a	64.2	25.3	36.3	2.53	91.1	0.9
HS01b	117.3	47.8	89.3	2.47	90.6	0.4
HS01c	381.5	131.1	315.2	2.90	90.6	1.3

The Table 4.5 belongs to the HS02 sample, which is fabricated on annealed Bi2212 crsytal. The onsets of critical temperature of the mesas are 92.7, 92.5 and 91.3 K for the mesa areas of 300×50, 200 × 50 and 100 × 50 μm^2, respectively. The $R_{(Tc)}/R_{(300\ K)}$ values are 1.14, 1.20 and 1.42, respectively.

Table 4.5. Electrical properties of HS02

	$R_{Tc(onset)}$ (ohm)	$R_{300\ K}$ (ohm)	$R_{contact}$ (ohm)	$R_{(Tc)}/R_{300K}$	$T_{c(onset)}$ (K)	ΔT_c (K)
HS02a	13.5	11.8	5.10	1.14	92.7	2.6
HS02b	16.8	13.9	3.9	1.20	92.5	2.4
HS02c	36.1	25.3	3.9	1.42	91.3	4.7

In addition, both $R_{(Tc)}/R_{(300\ K)}$ and the superconducting transition temperatures are consistent with the nearly underdoped state of the Bi2212 crystals.

The Table 4.6 represents the electrical properties of annealed Bi2212 crystal. The crystal is annealed at 450 ^{o}C for 4 hours. When we look at the Table 4.5, the transition temperatures of the mesas are the same as 85 K.

Table 4.6. Electrical properties of HS11

	$R_{Tc(onset)}$ (ohm)	$R_{300\ K}$ (ohm)	$R_{contact}$ (ohm)	$R_{(Tc)}/R_{300K}$	$T_{c(onset)}$ (K)	ΔT_c (K)
HS11a	25	8.4	1.8	1.95	85	12.0
HS11b	46	17	2.9	2.46	85	2.0
HS11c	75	24	4.3	2.50	85	4.3

The figures from Figure 4.9 to 4.20 represent the R-T characteristics of mesa structures. The R-T curves provide information about the doping level, contact resistance and quality of the crystal on which the mesa structure are fabricated. All fabricated mesas show some contact resistance even below the transition temperature as seen in the R-T curves. This kind of resistance generally can be eliminated; however, it is not preferred since it causes some differences in the oxygen doping level of Bi2212.

Moreover, as we see, all R-T graphs exhibit semiconductor like curves, which is observed below certain oxygen concentration in Bi2212 crystals. For this reason, some

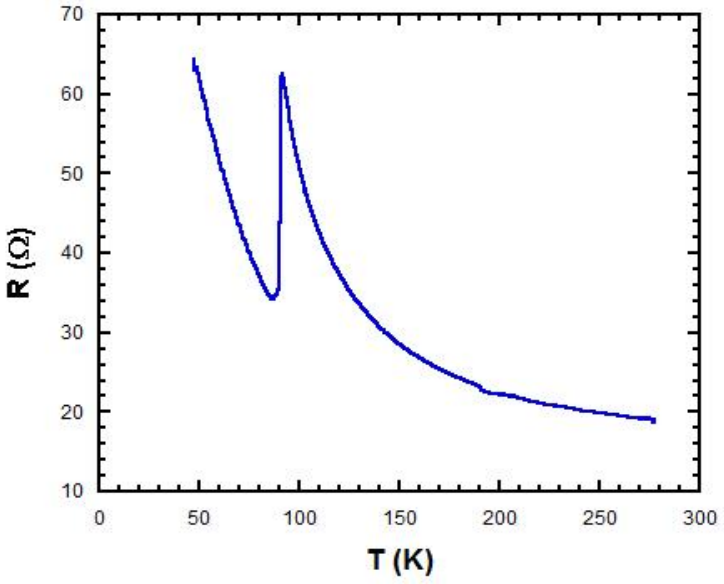

Figure 4.9. Resistance versus temperature behavior of HS01a

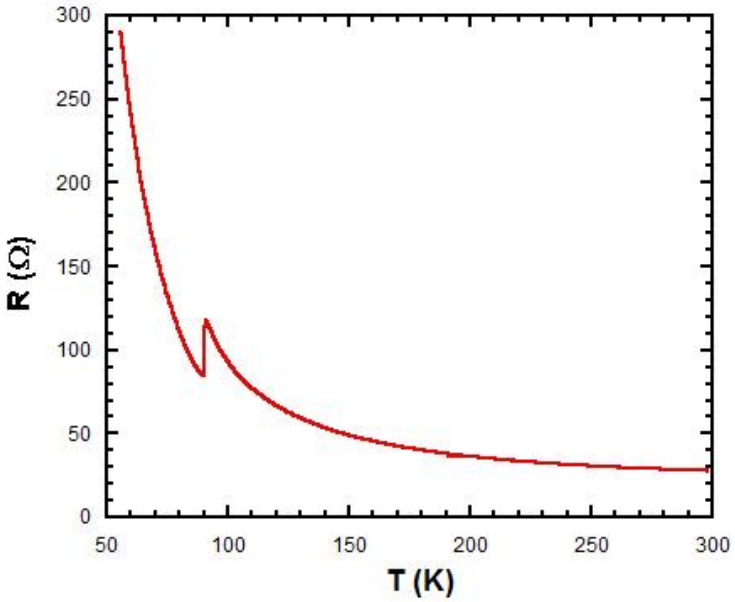

Figure 4.10. Resistance versus temperature behavior of HS01b

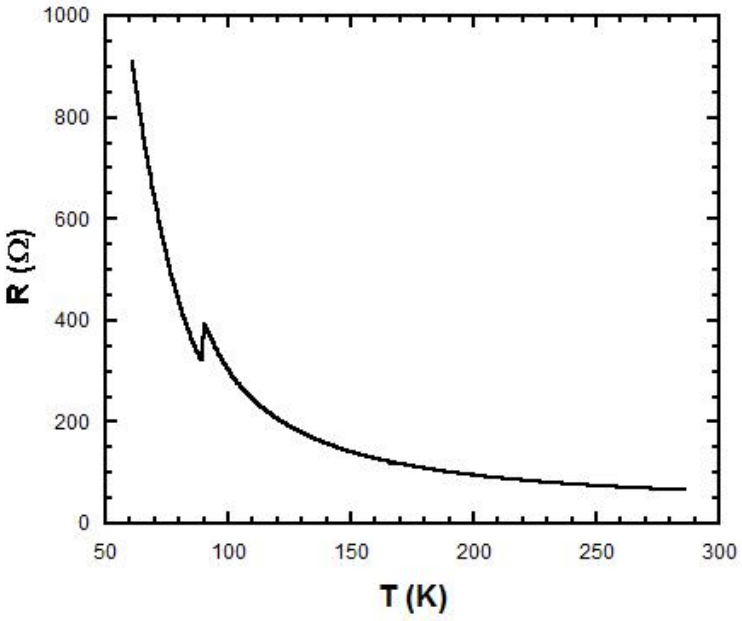

Figure 4.11. Resistance versus temperature behavior of HS01c

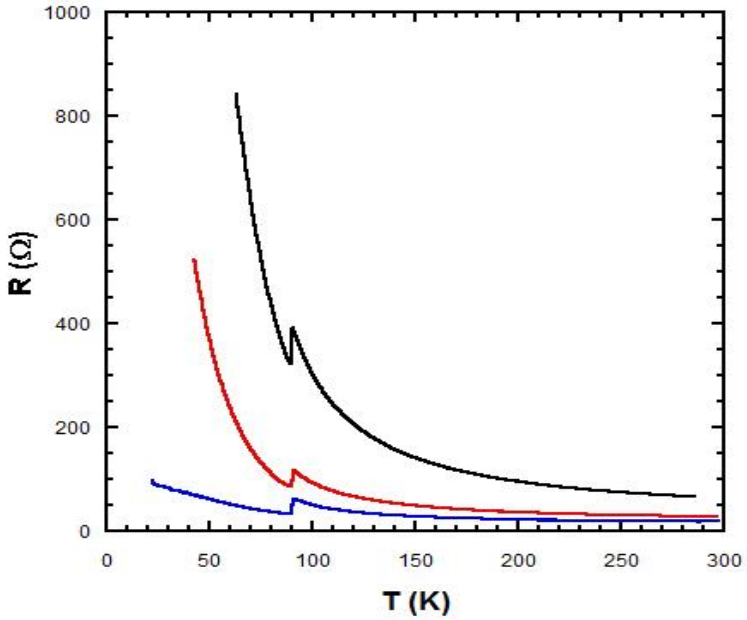

Figure 4.12. Resistance versus temperature behavior of all samples together

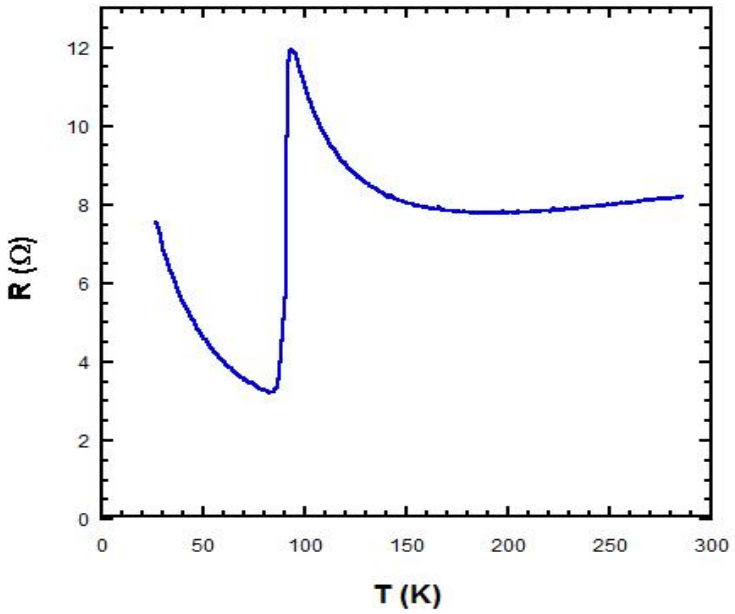

Figure 4.13. Resistance versus temperature behavior of HS02a

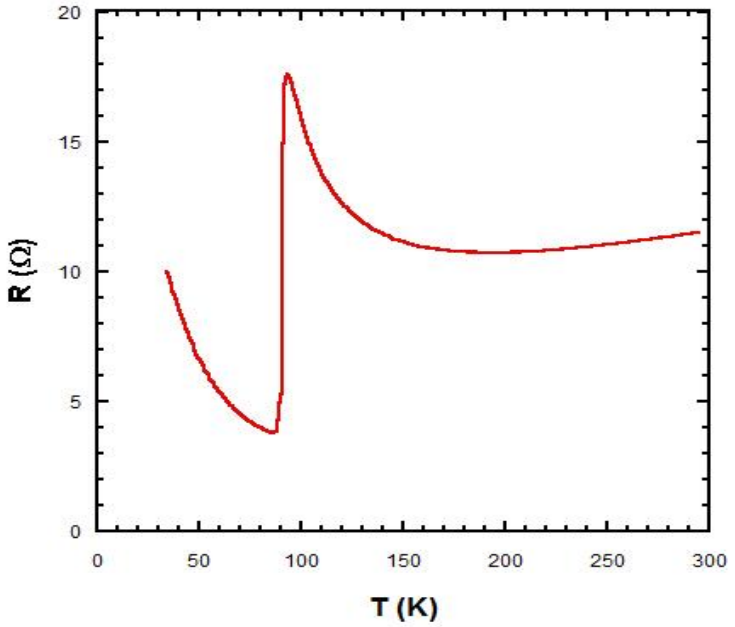

Figure 4.14. Resistance versus temperature behavior of HS02b

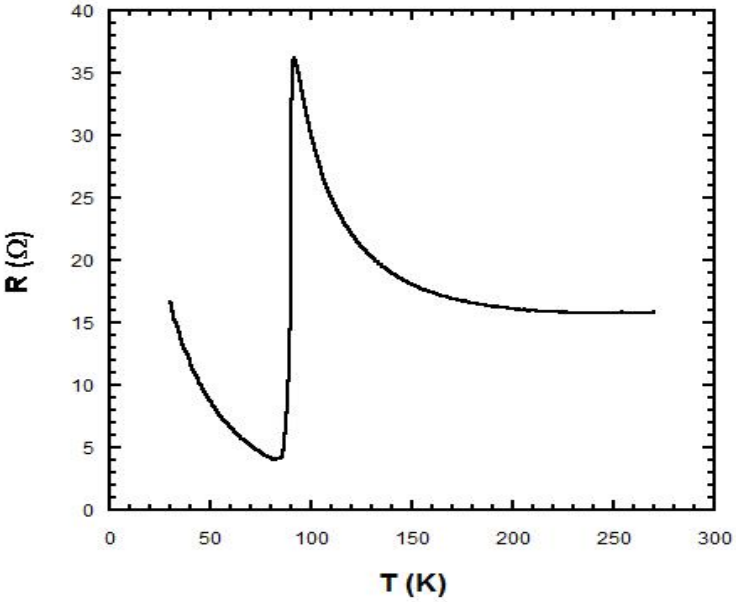

Figure 4.15. Resistance versus temperature behavior of HS02c

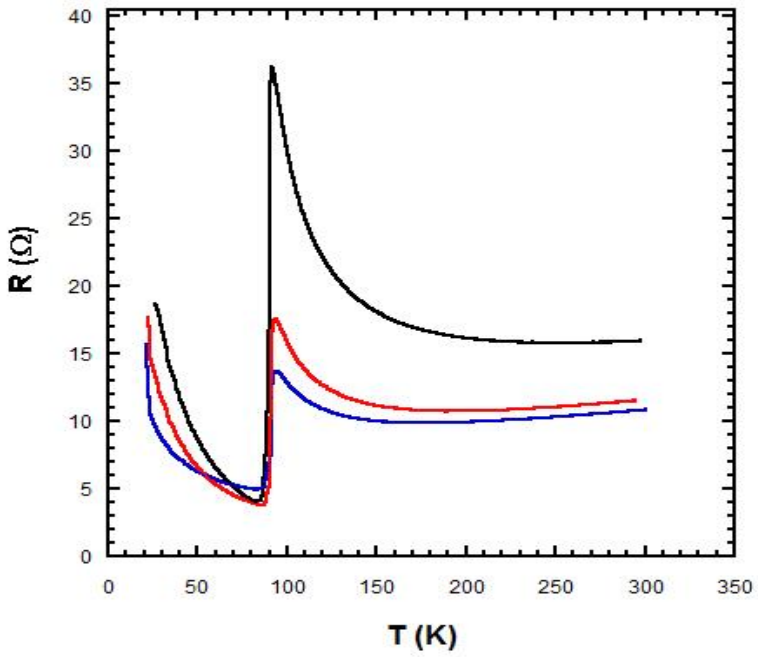

Figure 4.16. Resistance versus temperature behavior of all samples together

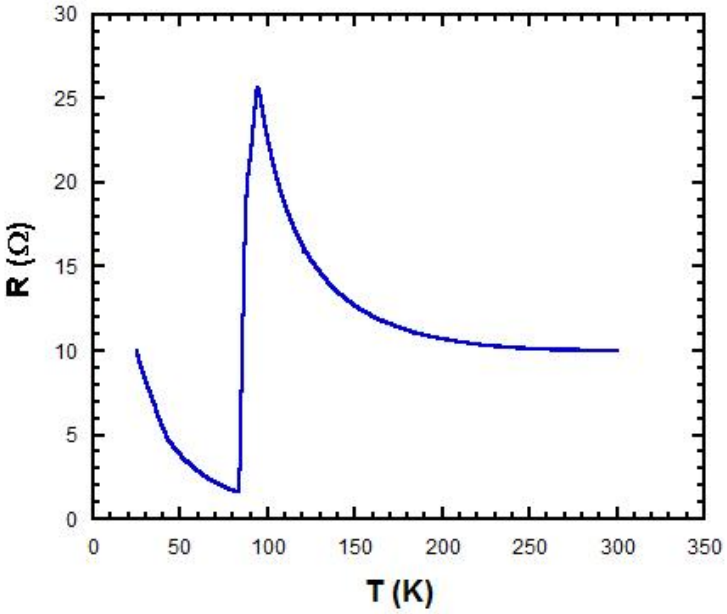

Figure 4.17. Resistance versus temperature behavior of HS11a

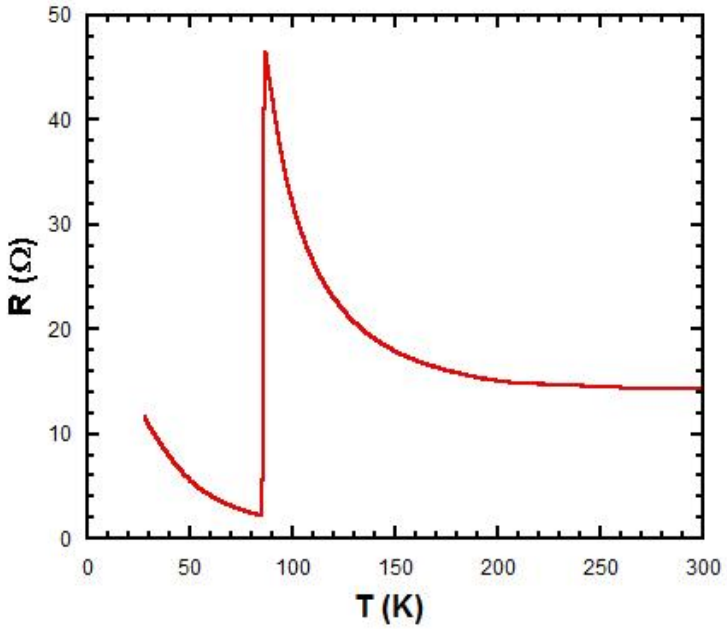

Figure 4.18. Resistance versus temperature behavior of HS11b

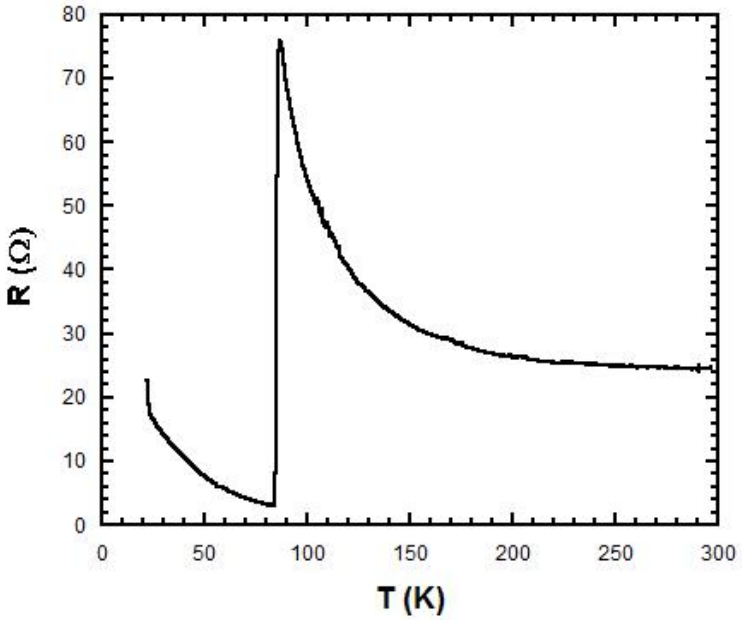

Figure 4.19. Resistance versus temperature behavior of HS11c

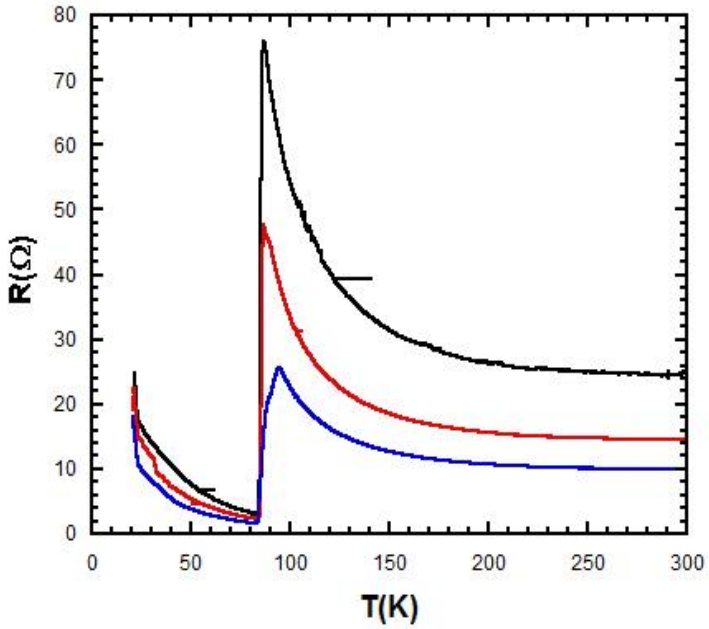

Figure 4.20. Resistance versus temperature behavior of all samples together

superconductor properties such as critical current density and transition temperature can be changed by altering the doping level. In addition to that, the structural and flux pinning properties of the high temperature superconductors cuprates vary by doping level. Moreover, doping is very important to understand the mechanism of high temperature superconductors.

When we see the Figure 9, Figure 10 and Figure 4.11, the contact resistances below the transition temperature are very high such as higher than 30 ohm. This is because of the interface between gold layer and surface of the Bi2212. In addition, this kind of resistance is increasing at very low temperature as seen in the figures. However, Figure 4.13, Figure 4.14 and Figure 4.15 that belong to HS02 sample and Figure 4.17, Figure 4.18 and Figure 4.19 that belong to HS11 show very low contact resistance approximately 5 ohm.

We observe that the overall magnitude of c-axis resistivity of the crystal increases with decreasing doping level. At variation of oxygen level from the optimally doped to overdoped, c-axis resistivity of the crystal gradually start to exhibit metallic behavior. Furthermore, the effect of the doping level can be seen in the transition temperature values. For instance, while the transition temperature is about 90 K for HS02 sample, it is about 85 K for HS11.

4.2.2 Tunneling Characteristic of Bi2212 Single Crystal

In this work, we have studied change in Josephson critical current density of mesas with different dimensions. For this reason, the I-V measurements were taken at 20 K to find the Josephson critical current values to obtain the area dependence of Josephson critical current density in superconducting Bi2212 mesas for terahertz emission.

The I-V measurements were taken at 20 K. Some quasiparticle branches are observed in the I-V characteristics as obviously seen in the Figure 4.23, Figure 4.25, Figure 4.27 and Figure 4.28. While the bias voltage increases, these branches appear in such a voltage jump until all IJJs are completely in normal state. While the bias voltage is decreasing, I-V data does not show these branches because there is a transition from normal state to superconducting state. This leads to hysteresis behaviour in the I-V characteristics.

In addition, we have seen that while the mesa dimension is increasing, the back bending of the current-voltage curve is seen due to the large volume of the mesa causes self-heating. The result of heating effects can be seen in the I-V curves as backbending.

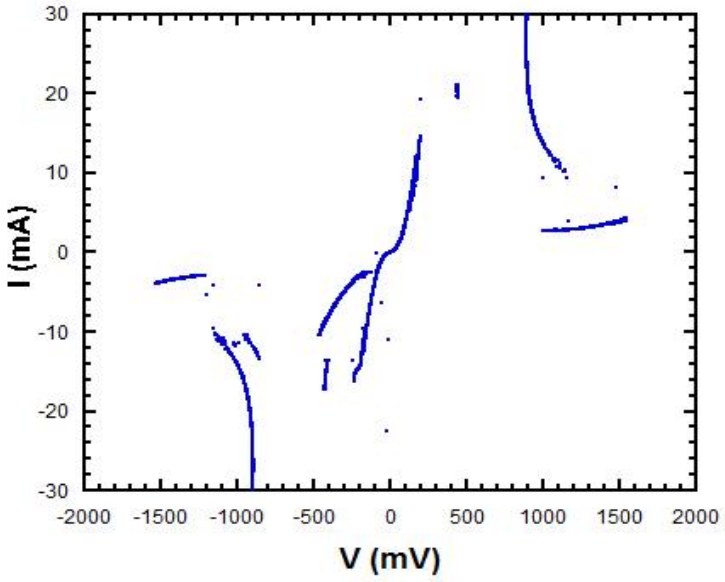

Figure 4.21. I-V measurement of HS01a at 20 K

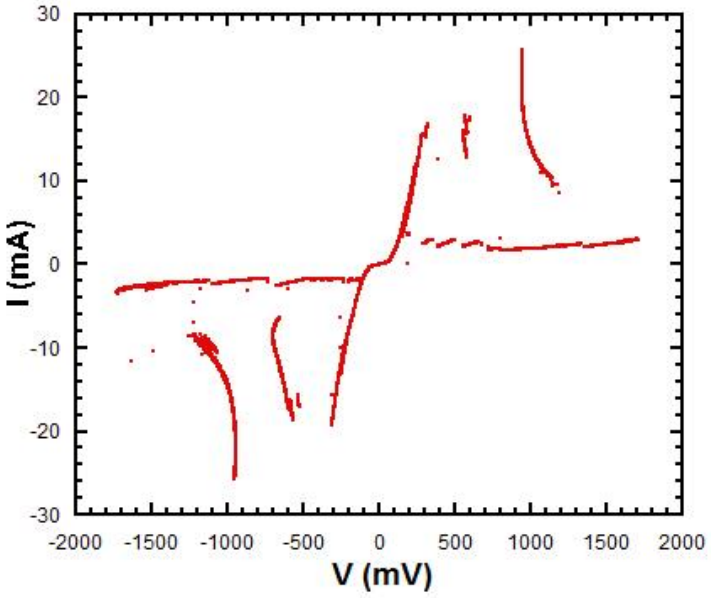

Figure 4.22. I-V measurement of HS01b at 20K

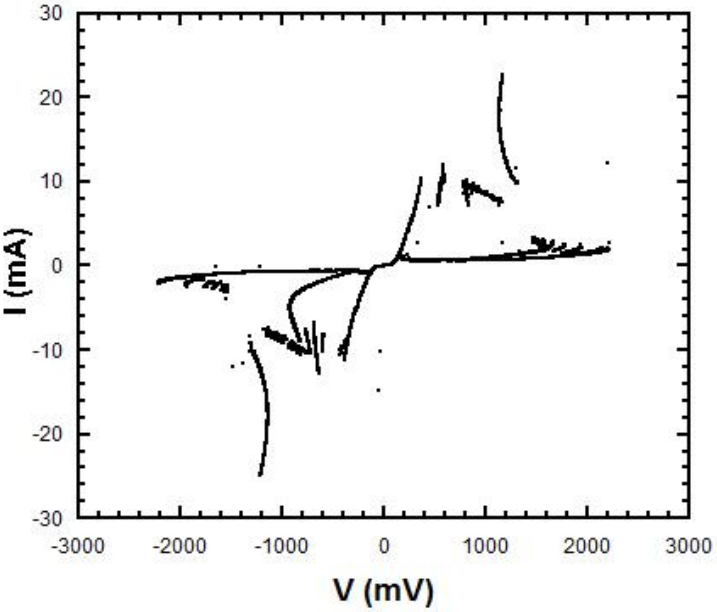

Figure 4.23. I-V measurement of HS01c at 20K

The Figure 4.21, Figure 4.22 and Figure 4.23 represent the I-V measurement of HS01a, HS01b and HS01c, respectively. The I-V measurements were taken at 20 K. The mesa dimensions for this sample can be seen in the Table 4.6. The I-V curves show several branches because of the individual switching of each junction from superconductor state to normal state when the bias current is bigger than the individual

critical current of each junction (Yurgens 2000). It means that each junction behaves like a single branch. In order to obtain all the branches, we swept the bias voltage positively and negatively many times.

In this work, we have studied change in Josephson critical current density of mesas with different dimensions. For this reason, the I-V measurements were taken at 20 K to find the Josephson critical current values to obtain the area dependence of Josephson critical current density in superconducting Bi2212 mesas. For HS01 sample, the magnitudes of Josephson critical currents of Bi2212 single crystal are about 12, 15.5, 10 mA, respectively. Then we have calculated the critical current densities of each mesa as 80, 155 and 400 A/cm^2, respectively. Therefore, we can conclude that the critical current density is decreasing when area of mesa is increasing. In addition, the backbending points are increasing while the mesa dimension is decreasing as seen in the Table 4.6.

Table 4.6 Electrical properties of HS01

	Mesa Dimensions (μm^2)	**I_c (mA)**	**J_c (A/cm^2)**	**Backbending point (mV)**
HS01a	300×50	12.0	80	1555
HS01b	200× 50	15.5	155	1750
HS01c	100 ×50	10.0	400	2000

Figure 4.24, Figure 4.25 and Figure 4.26 illustrate the I-V characteristics of HS02 sample. The I-V measurements also were taken at 20 K. Due to some measurement problems such as high swept frequency and quick increasing in amplitude of function generator output less quasiparticle branches are seen in some of our measurements. Nevertheless, general aspect reveals the heating effects.

In order to obtain as much as more quasiparticle branches in a I-V graph, the swept frequency should be low while ac bias current on mesa is swept negatively and positively by function generator. In addition, temperature dependence of c-axis tunneling characteristic of Bi2212 single crystals was analyzed by I-V measurements done at some constant temperatures. It can be concluded from the Figure 4.24, Figure

4.25 and Figure 4.26 that the magnitude of Josephson critical current densities for HS02 samle are 140, 160 and 180 A/cm^2, respectively. So we see again that the critical current density is decreasing when area of mesa increasing again mesa with nearly underdoped crystal. Furthermore, the backbending voltage points are increasing since heating effects dominate for the large areas of the mesa structures as seen in the I-V curves of HS02 sample.

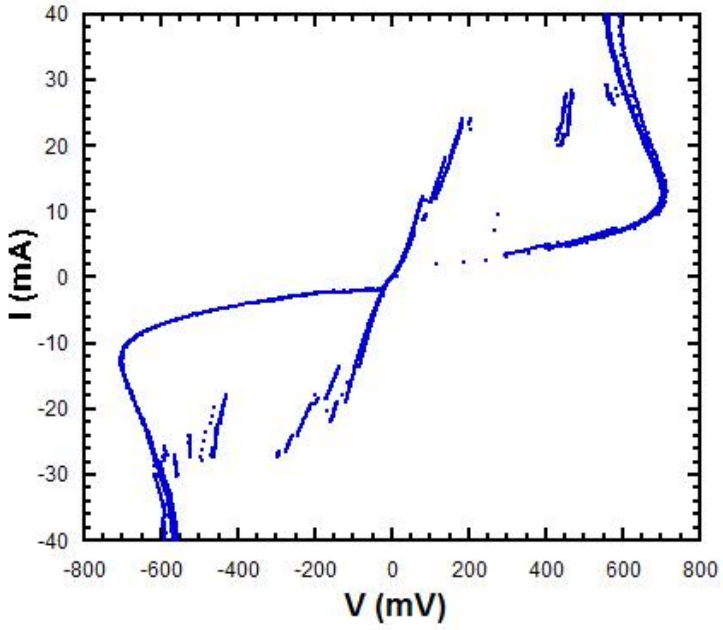

Figure 4.24. I-V measurement of HS02a at 20K

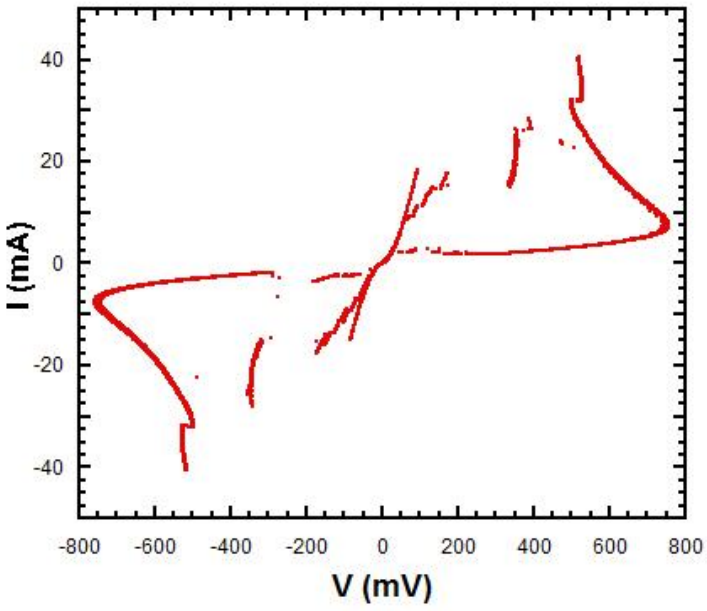

Figure 4.25. I-V measurement of HS02b at 20K

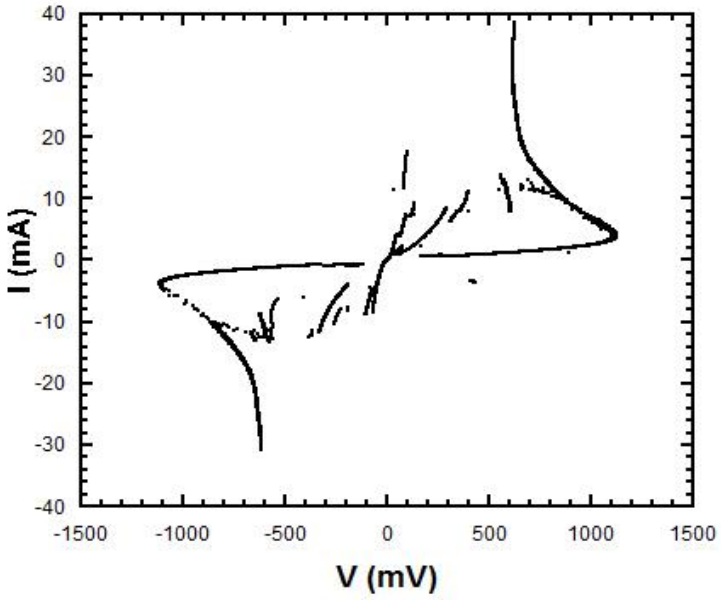

Figure 4.26. I-V measurement of HS02c at 20K

Table 4.8. I-V characteristics of HS02

	Mesa Dimensions (μm^2)	**I_c (mA)**	**J_c (A/cm^2)**	**Backbending point (mV)**
HS02a	300×50	21.8	140	720
HS02b	200× 50	18.4	160	760
HS02c	100 ×50	9	180	1120

The Figure 4.27, Figure 4.28 and Figure 4.29 represent the I-V measurement of HS11 sample, which is annealed at 450 ^oC for 4 hours. Especially, the Figure 29 belongs to mesa with area of 100 × 50 μm^2, shows many quasiparticle branches. We can see that the critical current of the fabricated mesas are 10.03, 8.05 and 5.03 mA for HS11a, HS11b and HS11c, respectively. Therefore, we can calculate the Josephson critical current densities as 60, 80 and 100 A/cm^2 for HS11a, HS11b and HS11c samples.

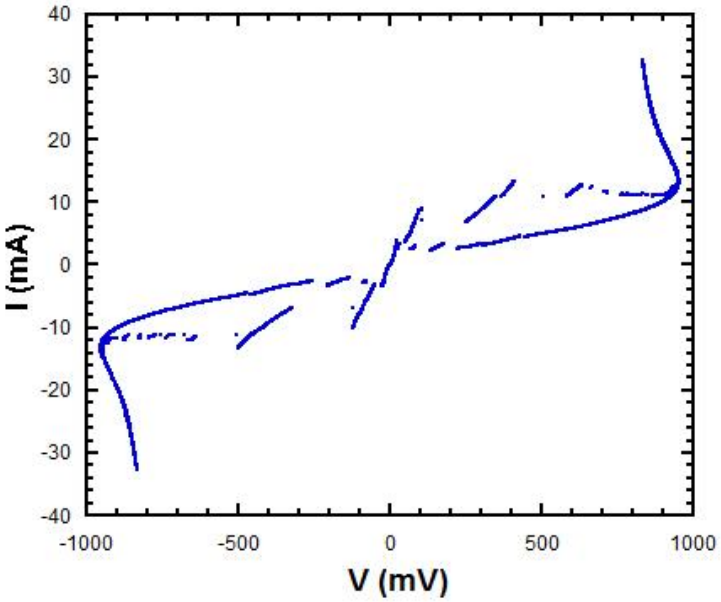

Figure 4.27. I-V measurement of HS11a at 20K

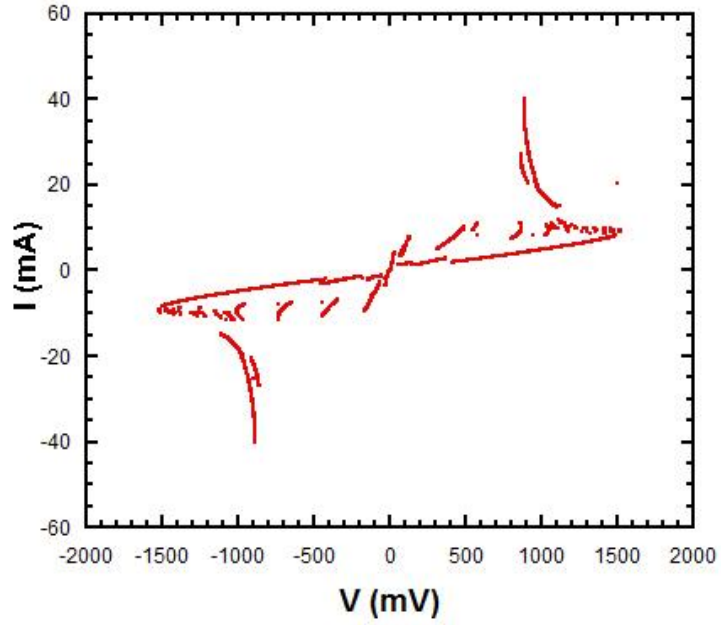

Figure 4.28. I-V measurement of HS11b at 20K

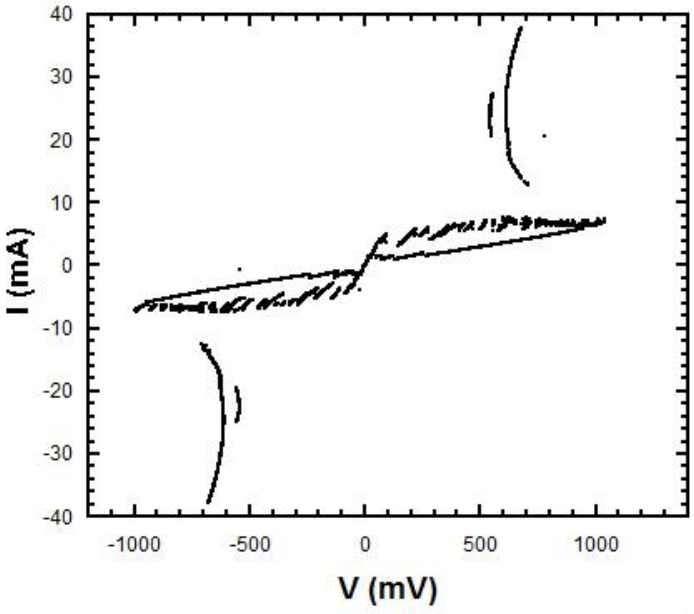

Figure 4.29. I-V measurement of HS11c at 20K

Furthermore, it is seen that the backbending voltage points are 1000, 1522, 1038 mV for HS11a, HS11b and HS11c samples. The backbending of the I-V curve at high voltages is due to self-heating effects as indicated by the appearance of unpolarized blackbody radiation (Ozyuzer, et.al. 2007).

Table 4.9. I-V characteristics of HS11

	Mesa Dimensions (μm^2)	**I_c (mA)**	**J_c (A/cm^2)**	**Backbending point (mV)**
HS11a	300×50	10.03	60	1000
HS11b	200× 50	8.05	80	1522
HS11c	100 ×50	5.03	100	1038

Some researchers have used several methods to reduce the heating effects such as reduction of the current density by intercalation of some molecules such as HgB_2, HgI_2, I_2 within the Bi-O bilayer, which increase the c-axis resistance. In addition, using short pulses and decreasing the mesa dimensions are other methods to decrease the self-heating effects In addition, in the all I-V curves, the large current density and close

proximity of neighboring junctions in Bi2212 junction arrays are interpreted as the cause of such heating effects.

CHAPTER 5

CONCLUSION

Rapid increase in applications of the electromagnetic waves in the terahertz frequency range requires new techniques to obtain continues-wave terahertz radiation sources. For this reason, we have fabricated triple mesa structures from Bi2212 single crystal using e-beam lithography and argon ion beam etching techniques. Our aim was to find the critical current density dependence of mesa area to obtain maximum emission power for the terahertz radiation.

Before starting the mesa fabrication process, we have used annealed and as grown Bi2212 single crystal for fabrication of triple mesa structures. First of all, these annealed single crystals were glued on sapphire substrates using good thermal and electrical conductor silver epoxy. Then we obtained smooth and clean surface of Bi2212 by cleaving process. After that 100 nm of gold layer is deposited onto cleaved crystals to protect them from chemical reaction. To obtain natural IJJ stacks with various size and height, mesa on Bi2212 have been fabricated using e-beam lithography and argon ion beam etching techniques. Since obtained mesas have small area, we have deposited CaF_2 insulating layer onto them. Then using lift off technique by e-beam lithography, we gold stripes with the width of 30 μm were deposited on insulating layer and mesa. Finally three gold wire in placed using silver epoxy.

After the mesa fabrication, surface profilometer and atomic force microscope were used to obtain the exact dimensions of each mesa. In order to characterize the Bi2212 mesas, three probe contacts were placed to measure c-axis resistance versus temperature (R–T), and current–voltage behavior (I-V) were measured in a He flow cryostat. When we look at the R-T graphs, we have observed that all fabricated mesas shows characteristic resistance versus temperature properties of c-axis of Bi2212 high temperature superconductors. It is seen from the graphs that the resistance is exponentially increasing when the temperature decrease from room temperature to 20K. While the onsets of the critical temperatures are generally between 85 K and 92 K, $R_{Tc}/R_{300\ K}$ values are between. Also when we look at our results, we see that the contact resistance below transition temperature is still finite. This is because of the interface

between gold layer and Bi2212 crystal and the resistance is increasing below critical temperature since the interface acts like a tunneling barrier at low temperatures.

In this work, we have studied change in Josephson critical current density of mesas with different dimensions. For this reason, the I-V measurements were taken at 20 K to find the Josephson critical current values to obtain the area dependence of Josephson critical current density in superconducting B2212 mesas for terahertz emission. We can conclude from the fabricated triple mesas I-V measurements that the Josephson critical current density is decreasing when area of mesa is increasing. Furthermore, some of the quasiparticle branches are observed in the I-V characteristic. While the bias voltage increases these branches appear in such a voltage jumps until all IJJs are completely in normal state. While the bias voltage is decreasing, I-V data does not show these branches because there is a transition from normal state to superconducting state. This leads to hysteresis behaviour in the I-V characteristics. Also we have seen that while the mesa dimension is increasing, the back bending of the current-voltage curve is seen due to the large volume of the mesa causes self-heating. Furthermore, due to the heating, the spaces between quasiparticle branches become smaller when approaching to higher bias values.

REFERENCES

Anderson, J. R. and J. M. Rowell. 1963. Probable observation of the Josephson superconducting tunnel effect. *Physical Review Letters* 10:230

Barbara, P., A. B. Cawthorne, S. V. Shitov and C. J. Lobb. 1999. Stimulated Emission and Amplification in Josephson junction Arrays. *Physical Review Letters* 82:1963

Bardeen, J., L. N. Cooper and J. R. Schrieffer. 1957. The Theory of Superconductivity. Physical Review Letters 108:1175.

Bandyopadhyay. A., Study of Propagation And Detection Methods of Terahertz Radiation for Spectroscopy and Imaging, *New Jersey Institute of Technology Thesis of Ph.D.*

Batov, I. E., X. Y. Jin, S. V. Shitov, Y. Koval, P. Muller and A. V. Ustinov. 2006. Detection of 0.5 THz radiation from intrinsic $Bi_2Sr_2CaCu_2O_{8+x}$ Josephson junctions. *Applied Physics Letters* 88:262504.

Bednorz, J. G. and K. A. Müller. 1986. Possible high Tc superconductivity in the Ba−La−Cu−O system. *Zeitschrift Physics* B 64:189-193.

Benseman, T., A. E. Koshelev, K. E. Gray, W.-K. Kwok, and U. Welp, K. Kadowaki and M. Tachiki, T. Yamamoto. 2011. Tunable terahertz emission from Bi2Sr2CaCu2O8+δ mesa devices. *Phys. Rev. B* 84: 064523.

Bulaevskii, L. N. and A. E. Koshelev. 2007. Radiation due to Josephson Oscillations in Layered Superconductors. *Physical Review Letters* 99:057002

Booske, J. H., R. J. Dobbs, C. D. Joye, C. L. Kory, G. R. Neil, G. Park, J. Park, and R. J. Temkin. Vacuum electronic high-power terahertz sources. *Ieee Transactıons On Terahertz Scıence And Technology* 1:54-75

Davies, A. G., E H Linfield and M B Johnston. 2002. The development of terahertz sources and their applications. *Phys. Med.Biol*. 47:3679–3689

Demirhan, Y. 2011. Fabrication Of Double Mesa Structures From Superconducting Bi2sr2cacu2o8+D by e-Beam Lithography for Terahertz Emission, *Izmir Institute of Technology Thesis of M.S*

Genoud., J.Y., Triscone G, Junod A and Muller. 1995. Reversible magnetization as a function of the oxygen concentration in Bi-2212 superconducting ceramics. *Physica C: Superconductivity* 242:143-154

Gray, K.E., L. Ozyuzer, A.E. Koshelev, C. Kurter, K. Kadowaki, T. Yamamoto, H. Minami, H. Yamaguchi, M. Tachiki, W.K. Kwok and U. Welp. 2009. Emission of Terahertz Waves from Stacks of Intrinsic Josephson Junctions. *IEEE Transactions on Applied Superconductivity* 19:886

Irie, A., Y. Hirai and G. Oya. 1998. Fiske and flux-flow modes of the intrinsic Josephson junctions in Bi2Sr2CaCu2Oy mesas. *Applied Physical Letters* 72:2159

Jain, A. K., K. K. Likharev, J. E. Lukens and J. E. Sauvageau. 1984. Mutual phase-locking in Josephson junction arrays. *Physics Reports* 109:309

Josephson, B. D. 1962. Possible new effects in superconductive tunneling. *Physics Letter* 1:251-253.

Josephson, B. D. 1964. Coupled Superconductors. *Review of Modern Physics* 36:216–220.

Josephson, B. D. 1974. The discovery of tunnelling supercurrents. *Review of Modern Physics* 46(2):251-254.

Kadowaki, K., I. Kakeya, T. Yamamoto, T. Yamazaki, M. Kohri and Y. Kubo. 2006. Dynamical properties of Josephson vortices in mesoscopic intrinsic Josephson junctions in single crystalline Bi2Sr2CaCu2O8+d. *Physica C* 437-438:111-117.

Kadowaki, K., H. Yamaguchi, K. Kawamata, T. Yamamoto, H. Minami, I. Kakeya, U. Welp, L. Ozyuzer, A. Koshelev, C. Kurter, K. E. Gray and W. K. Kwok. 2008. Direct observation of terahertz electromagnetic waves emitted from intrinsic Josephson junctions in single crystalline Bi2Sr2CaCu2O8+d. *Physica C* 468:634-639 .

Kadowaki, K., M. Tsujimoto, K. Yamaki, T. Yamamoto, T. Kashiwagi, H. Minami, M. Tachiki and R. A. Klemm. 2010. Evidence for a Dual-Source Mechanism of Terahertz Radiation from Rectangular Mesas of Single Crystalline Bi2Sr2CaCu2O8+δ Intrinsic Josephson Junctions. *Journal of the Physical Society of Japan* 79: 023703.

Kakeya I, Y. Omukai, T.Yamamoto, K. Kadowaki and M. Suzuki. 2012 *Applied Physics Letters* 100: 242603.

Khalil, S. M. 2000. Effects of Optimum Annealing Time on Superconducting Properties of Bi2-xPbxSr2Ca2Cu3Oy. *System Phys. Stat. Sol*. 178-731.

Kleiner R., F. Steinmeyer, G. Kunkel, and P. Müller. 1992. Intrinsic Josephson effects in Bi2Sr2CaCu2O8 single crystals. *Physical Review Letters* 68:2394.

Kleiner, R. 1994. Two-dimensional resonant modes in stacked Josephson junctions. *Physical Review B* 50:6919.

Koshelev, A. E. and I. Aranson. 2001. Dynamic structure selection and instabilities of driven Josephson lattice in high-temperature superconductor. *Physical Review B* 64:174508.

Koshelev A. E. and L. N. Bulaevskii. 2008. Resonant electromagnetic emission from intrinsic Josephson junction stacks with laterally modulated Josephson critical current. *Physical Review B* 77:014530.

Krasnov, V. M. 2006. Quantum Cascade Phenomenon in $Bi_2Sr_2CaCu_2O_{8+\delta}$ Single Crystals. *Physical Review Letters* 97:257003.

Kresin, V. Z., Stuart A. Wolfb, Yu.N. Ovchinnikovc, Exotic normal and superconducting properties of the high-Tcoxides, *Physics Reports* 288:347-354.

Kume, E. I., Iguchi, and H. Takahashi. 1999. On-chip spectroscopic detection of terahertz radiation emitted from a quasiparticle-injected nonequilibrium superconductor using a high-T_c Josephson junction. *Applied Physics Letters* 75: 2809.

Kurter, C., K. E. Gray, J. F. Zasadzinski, L. Ozyuzer, A. E. Koshelev, Q. Li, T. Yamamoto, K. Kadowaki, W. K. Kwok, M. Tachiki and U. Welp. 2009. Thermal Management in Large Bi2212 Mesas Used for Terahertz Sources. *IEEE Transactions on Applied Superconductivity* 19: 428

Kurter, C., L. Ozyuzer, T. Proslier, J. F. Zasadzinski, D. G. Hinks and K. E. Gray. 2010. Counterintuitive consequence of heating in strongly-driven intrinsic junctions of Bi2Sr2CaCu2O8 mesas. *Physical Review B* 81: 224518.

Langenberg, D. N., D. J. Scalapino, B. N. Taylor, and R. E. Eck. 1965. Investigation of Microwave Radiation Emitted by Josephson Junctions. *Physical Review Letters* 15: 294.

Lee Y.S,. 2009. Principles of Terahertz Science and Technology, *Springer Science+Business Media,LLC*, New York

Leyraud, N.D., C. Proust, D. LeBoeuf, J. Levallois, J. B. Bonnemaison, R. Liang , D. A. Bonn, W. N. Hardy and L. Taillefer.2007. Quantum oscillations and the Fermi surface in an underdoped high-Tc superconductor, *Nature* 447: 565-568

Maeda, H., T. Tanaka, M. Fukutomi and T. Asano. 1988. A New high-Tc oxide superconductor without a rare earth element. *Japanese Journal of Applied Physics* 27: L209.

Madsen, S., G. Fillatrella, and N. F. Pedersen. 2004. Interaction between a BSCCO-type intrinsic Josephson junction and a microwave cavity. *European Physical Journal B* 40: 209.

Meissner, W. and R. Ochsenfeld. 1933. Ein neuer effect bei eintritt der supraleitfahigkeit. *Naturwissenschaften* 21(44): 787.

Miyakawa, N., P. Guptasarma, J.F. Zasadzinski, D.G. Hink and K.E. Gray. 1998. Strong dependence of the Superconducting gap on oxygen doping fromtunneling measurements on Bi2Sr2CaCu2O8+x. *Physical Review Letters* 80:157.

Onnes, H. K. 1911. Disappearance of the electrical resistance of mercury of Helium temperature. *Akad. Van Wetenschappen (Amsterdam)* 14: 113.

Ozyuzer, L., A. E. Koshelev, C. Kurter, N. Gopalsami, Q. Li, M. Tachiki, K. Kadowaki, T. Tamamoto, H. Minami, H. Yamaguchi, T. Tachiki, K. E. Gray, W. K. Kwok and U. Welp. 2007. Emission of coherent THz radiation from superconductors. *Science* 318: 1291.

Ozyuzer, L., Y. Simsek, H. Koseoglu, F. Turkoglu, C. Kurter, U. Welp, A. E. Koshelev, K. E. Gray, W. K. Kwok, T. Yamamoto, K. Kadowaki, Y. Koval, H. B. Wang, and P. Müller. 2009. Terahertz wave emission from intrinsic Josephson junctions in high-Tc superconductors. *Superconductor Science & Technology* 22: 114009.

Rogalskii, A. and F. Sizov. 2011. Terahertz detectors and focal plane arrays. *Opto−Electronics Review* 19:346-404.

Suzuki, M., T. Hamatani, Y. Yamada, K. Anagawa and T. Watanabe. 2009. Significantly doping-dependent Josephson critical current–inhomogeneity in real space or heterogeneity in k-space. *Journal of Physics: Conference Series* 150: 052252.

Tachiki, M., S. Fukuya and T. Koyama. 2009. Mechanism of Terahertz Electromagnetic Wave Emission from Intrinsic Josephson Junctions. *Physical Review Letters* 102:127002.

Tsujimoto M., K. Yamaki, K. Deguchi, T. Yamamoto, T.Kashiwagi, H. Minami, M. Tachiki, and K. Kadowaki. 2010. Geometrical Resonance Conditions for THz Radiation from the Intrinsic Josephson Junctions in Bi2Sr2CaCu2O8+δ. *Phys. Rev. Lett*. 105: 037005.

Tsujimoto M., T. Yamamoto, K. Delfanazari, R. Nakayama, T. Kitamura, M. Sawamura, T. Kashiwagi, H.Minami, M. Tachiki, K. Kadowaki,and R. A. Klemm. 2012. Broadly Tunable Sub-terahertz Emission from Internal Branches of the Current-voltage Characteristics of Superconducting Bi2Sr2CaCu2O8+δ Single Crystals. *Phys. Rev. Lett*. 108: 107006.

Tonouchi, M. 2007. Cutting-edge terahertz technology. *Nature Photonics* 1:97-105.

Turkoglu F., H. Koseoglu, Y. Demirhan, L. Ozyuzer, S. Preu, S. Malzer, Y. Simsek, P. Muller, T. Yamamoto and K. Kadowaki. 2012. Interferometer measurements of terahertz waves from Bi2Sr2CaCu2O8+d mesas. *Supercond. Sci. Technol*. 25 (12): 125004

Turkoglu F., L. Ozyuzer, H. Koseoglu, Y. Demirhan, S. Preu, S. Malzer,Y. Simsek, H.B. Wang, P. Muller. 2013. Emission of the THz waves from large area mesas of superconducting Bi2Sr2CaCu2O8+d by the injection of spin polarized current. *Physica C: Superconductivity* 491: 7-10.

Yamaki. K., M. Tsujimoto, T. Yamamoto, A. Furukawa, T. Kashiwagi, H. Minami, K. Kadowaki. 2011. High-power terahertz electromagnetic wave emission from high-Tcsuperconducting Bi2Sr2CaCu2O8+δ mesa structures. *Optics Express* 19: 3193.

Yurgens, A. 2000. Intrinsic Josephson junctions: Recent developments. *Superconductor Science and Technology* 13: R85-100.

Wang, Y., L. Li, M. J. Naughton, G. D. Gu, S. Uchida, and N. P. Ong. 2005. Field-Enhanced Diamagnetism in the Pseudogap State of the Cuprate Bi2Sr2CaCu2O8 Superconductor in an Intense Magnetic Field. *Physical Review Letters* 95, 247002.

Wang H. B., S. Guenon, J. Yuan, A. Iishi, S. Arisawa, T. Hatano, T. Yamashita, D. Koelle and R. Kleiner. 2009. Hot Spots and Waves in $Bi_2Sr_2CaCu_2O_8$ Intrinsic Josephson Junction Stacks: A Study by Low Temperature Scanning Laser Microscopy. *Physical Review Letters* 102:017006

Watanabe T., T. Fuji and A. Matsuda. 1997. Anisotropic resistivities of precisely oxygen controlled single-crystal Bi2Sr2CaCu2O8+d: Systematic study on "Spin Gap" effect. *Physical Review Letters* 79:2113.

Wade, A., G. Fedorov, D. Smirnov, S. Kumar, B. S. Williams, Q. Hu and J. L. Reno. 2009. Magnetic-field-assisted terahertz quantum cascade laser operating up to 225 K. *Nature Photonics* 3: 41.